Electron transport in quantum well infrared photodetectors

Thesis by
Ali Shakouri

In Partial Fulfillment of the Requirements
for the Degree of
Doctor of Philosophy

California Institute of Technology
Pasadena, California

1996

(Submitted July 20,1995)

Acknowledgments

I would like to express my sincere gratitude to my adviser, Prof. Amnon Yariv, for his encouragement and support throughout my graduate studies at Caltech. His keen scientific intuition has been a constant inspiration, and it has been a privilege to be a member of his highly motivated and talented quantum electronics group.

I would like to thank Dr. Howard Chen, Ali Ghaffari, Prof. Ilan Gravé, Dr. Lars Eng and Naohiro Kuze for introducing me to the field of Molecular Beam Epitaxy (MBE). I will always remember the Many Beautiful Evenings that we spent also with Yoshiro Yamada and John O'Brien, working on the Most Broken Equipment! I am indebted to Ali Ghaffari for his friendship, advice, and technical assistance with the crystal growth and device fabrication throughout my research projects. His help, often beyond the duties of a research engineer, made possible, and easier, much of the experimental work presented in this thesis.

Special thanks to Prof. Ilan Gravé who introduced me to the field of quantum well infrared photodetectors (QWIPs), and taught me the device processing and the detector characterization. Our collaboration on multi-color detectors during my first years at Caltech, was the basis for much of the transport study in subsequent years. I have also benefited from the extensive collaboration with Yuanjian Xu in the last two years, studying electrical and optical properties of QWIPs. His processing expertise and his careful experimental measurements were very valuable to finally explain several interesting results.

I have greatly enjoyed the collaboration and discussion with Gilad Almogy and John O'Brien on several projects (highly strained InGaAs/AlAs multiquantum wells, integrated quantum well detector and modulator, etc.).

Special thanks to Dr. Randy Salvatore for many stimulating discussions here at Watson, during conferences, and even during our job interviews! He also read the entire thesis and made many valuable suggestions. It was also a great pleasure to interact with other members of quantum electronics group: Drs. John Kitching, Richard

Boyd, Bin Zhao, Thomas Schrans, Tony Kewitsch, Profs. Gert Cauwenberghs and Moti Segev. We had many fruitful and enlightening discussions on various subjects ranging from device physics to the meaning of quantum mechanics!

I would like to express my appreciation to Kevin Cooper, Reynold Johnson, Paula Samazan and especially to Jana Mercado for her early-morning words of encouragement, kind support, and help in day-to-day matters.

I am extremely grateful to Prof. Philippe Gallion from Ecole Notionale Supérieure de Télécommunication de Paris, Prof. Yves Guldner from Ecole Normale Supérieure, and Profs. Jean Pierre Gazeau and Jean Klein from Université de Paris 7, for their advice, encouragement and continuous support which made my studies at Caltech possible.

I thank Professors Bruno Crosignani, Demetri Psaltis, Axel Scherer, and Kerry Vahala for taking the time to be on my examination committee, and for their valuable advice on several occasions.

Finally my deepest gratitude goes to my parents, Shahram, Shahrokh, Shohreh and Maryam for their constant support, love and encouragement

Electron transport in quantum well infrared photodetectors

by

Ali Shakouri

In Partial Fulfillment of the
Requirements for the Degree of
Doctor of Philosophy

Abstract

In this work the technique of molecular beam epitaxy is used to grow $GaAs/AlGaAs$ multiquantum well structures. The material composition and thicknesses are chosen in a way that the electrons in the device interact resonantly with infrared radiation. This interaction originates from quantized energy states (subbands) in the conduction band of the material. The infrared absorption and photocurrent spectroscopies, in conjunction with standard DC-characterizations, are used to investigate electron transport in these structures.

After a brief description of electronic energy states based on the multi-band **k.p** approximation, the optical properties of intersubband transitions are theoretically and experimentally investigated. Evidence for the above-the-barrier energy states (continuum minibands) affecting the absorption and photocurrent spectra is presented.

Studying electron transport perpendicular to the multiquantum well layers, different regimes of miniband and hopping conduction are distinguished. It is shown that sequential resonant tunneling and electric field domain formation occur even in very weekly coupled quantum wells (separated by 44 nm barriers), its application to the design of voltage-controlled multi-color infrared detectors is discussed and demonstrated. Finally, the low bias behavior of quantum well detectors is analyzed and evidence for photocurrent flowing in the opposite direction to the applied bias is presented.

Contents

List of Figures

Chapter 1

Introduction

In the middle of the twentieth century the use of semiconductors revolutionized various aspects of information processing. This was due mainly to the fact that the semiconductor conductivity can be changed precisely and reproducibly by several orders of magnitude by doping or by varying some external parameters such as voltage and temperature. The introduction of the transistor and other semiconductor devices and circuits open the road for machines with a higher level of complexity including modern computers. The need for faster speeds of operation, given the limitations in the speed of carriers in available semiconductors, lead to the introduction of integrated circuits and smaller size of devices. On the other hand, for the transmission of information, the introduction of low loss fibers open the road for speed-of-light communications, and subsequently optoelectronic devices.

The availability of high precision growth of ultrathin layers of semiconductors through molecular beam epitaxy (MBE) and metal organic chemical vapor deposition (MOCVD), permitted the introduction of quantum devices and man-made semiconductors. With the thickness of these structures being smaller than the electron de Broglie wavelength in the material, the wave nature of carriers, as predicted by quantum mechanics, is manifested. The electron wave interference effects give another degree of freedom in designing various devices. Two most intriguing examples are quantum wells and superlattices, in the former the carrier motion in one dimension is

restricted by an ultrathin layer, limiting electron energies to a set of discrete values so that the boundary condition for a standing wave are satisfied; in the latter, the additional translational symmetry by a series of alternating thin layers, gives rise to the formation of minibands separated by energy gaps in the conduction and valence bands of the structure. Both of these effects, modifying the electronic density of states, dramatically change electrical and optical properties of the material.

1.1 Outline of the thesis

In this work the technique of molecular beam epitaxy (MBE) is used to grow multi-quantum well structures. The material composition and thicknesses are chosen in a way that the electrons in the device interact resonantly with infrared radiation. This interaction originates from quantized energy states in the conduction band of the material. As the material used in this study ($GaAs/AlGaAs$) has a conduction band with spherical s-type symmetry, electrons behave like free particles with an *effective* mass m^*. This permits study of how the electron transport is effected by the formation of energy levels originating from alternating layers of material, without worrying about the underlying individual atomic potentials which may be very complicated.

The infrared absorption and photocurrent spectroscopies, in conjunction with standard DC-characterizations, are used to investigate electron transport in these structures; and some of the applications such as multi-color tunable detectors are discussed. The presentation in this thesis is divided as follows:

In chapter two, the theory of epitaxial growth of ultrathin semiconductors is briefly mentioned, and important practical issues for MBE growth of high quality materials (involving UHV system, sample preparation and various characterizations) are presented.

Some theoretical background about modelling of electronic states in bulk semiconductors and heterojunctions, through envelope function approximation, are reviewed

in chapter three. The multi-band analysis of the electronic states reveals the differences between interband and intersubband transitions. A self-consistent solution of Schrödinger and Poisson equations is used to calculate electronic energy levels and wavefunctions in multiquantum wells. The absorption spectrum of bound-to-bound and bound-to-continuum quantum well infrared photodetectors are analyzed, with a particular attention to the role of continuum states above the barriers.

Chapter four outlines theory of electron transport perpendicular to the layers, in a multiquantum well structure. After a brief review of the classical and quantum theories of transport, two regimes of miniband and hopping conduction are distinguished. We will see how in both of these cases negative differential conductivity can give rise to instabilities and electric field domain formation.

In chapter five, evidences for sequential resonant tunneling and electric field domain formation in very weakly coupled quantum wells, are presented. Its application to the design of voltage-controlled multi-color infrared detectors are discussed.

And finally in chapter six, the low bias behavior of quantum well detectors is analyzed and evidence for photocurrent flowing in the opposite direction to the applied bias are presented.

Chapter 2

Molecular Beam Epitaxy

Molecular beam epitaxy (MBE) is one of several techniques for growing high quality thin films on a single crystal substrate. All of the devices and structures described in this thesis are grown using this method. In this chapter a brief description of the physics of epitaxial growth, MBE system, and various calibrations and characterizations are given.

2.1 Physics of epitaxial growth

Epitaxy, from the Greek words *epi* and *taxis* meaning "upon" and "ordered," is the ordered growth of a material upon a substrate. This refers to the growth of a single crystal in a unique crystal orientation on a single-crystal substrate either of the same or a foreign material [8,19,32]. It can be viewed as a two-step process consisting of the deposition of atoms onto the surface of the growing crystal and migration of these atoms into their proper lattice positions (see figure 2-1). Thus adsorption, desorption, diffusion and surface reactions are the relevant processes. The rate of adsorption is primarily determined by the incoming particle flux. Whereas desorption, diffusion and reactions are activated processes, so that temperature plays a crucial role on whether a quasi-equilibrium is maintained during the growth process or not.

The crystal growth is a non-equilibrium phenomenon whether in the stationary or

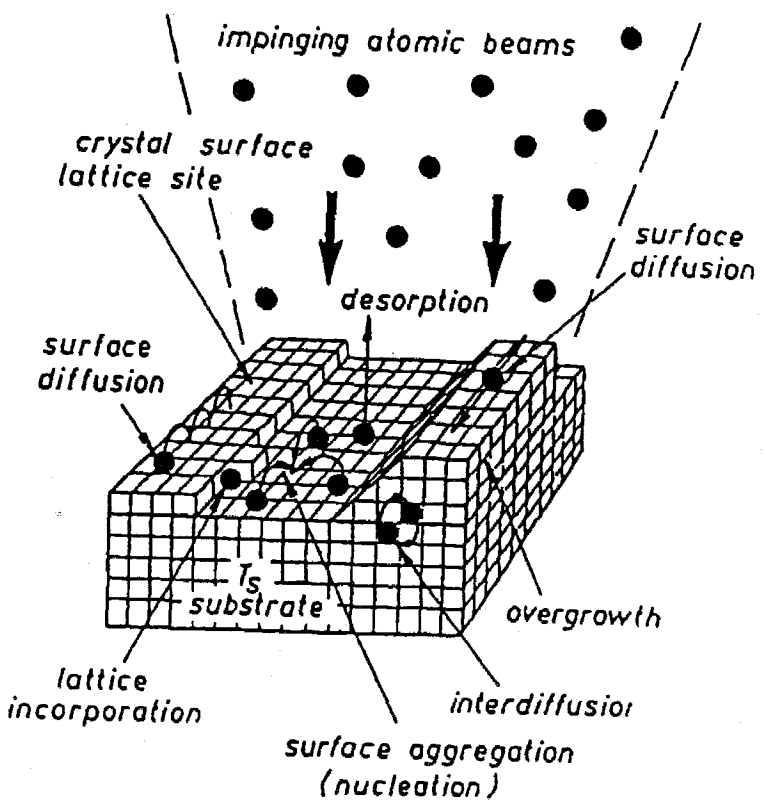

Figure 2-1: Various processes involved in the epitaxial growth: adsorption, desorption, diffusion and surface aggregation[19].

transient regime. However, growth conditions might be set so that at any stage the distribution of the atoms on the surface might be such that if an appropriate vapor pressure were established above the surface, no redistribution of atoms would occur. The layer-by-layer growth is assured by nucleation of condensed islands which grow together by migration of particles from the surrounding 2-d gas and adhere to the rim of the islands.

2.2 Molecular beam epitaxy

What is known today as MBE began in the 1960s following studies of evaporation rates and sticking coefficients of various elements on substrates [8]. As the name implies, in this case the material is supplied to the surface of the wafer as beams of molecules from thermal cells in a vacuum chamber. This contrasts with liquid phase epitaxy (LPE) in which the component materials are supplied from a metallic solvent bath, and chemical vapor deposition (CVD), in which the materials are supplied by a gas which reacts on the surface of the wafer to deposit the material.

One of the main virtues of the MBE technique is that since the materials are transported to the surface of the substrate by a collisionless beam (molecular beam), it is possible to modulate the incorporation of a material by simply imposing a shutter between the source of the beam and the growing layer. A typical growth rate during an MBE deposition is one atomic layer per second, or approximately one micron per hour, which means that a reasonably fast shutter action results in an atomically abrupt transition in the composition of the growing layer.

The difference between MBE and a simple vacuum evaporation deposition are the degree of elimination of contaminants in the source materials, in the vacuum chamber, and in the processing of the single crystal substrate which provides a nearly ideal terminated lattice. The growth is carried out at an elevated substrate temperature, allowing the deposited material to crystalize into the lattice provided by

the underlying substrate. In the case of compound semiconductors, it would seem an impossible task to supply the constituent materials at precisely the right ratio to grow a stoichiometric material. In this case, use is made of the fact that one of the elements involved is usually much more volatile than the other at the substrate growth temperature (The group V element in the case of III-V semiconductors.). This allows an excess of that material to be supplied to the surface. That which is not immediately incorporated in the growing semiconductor is then re-evaporated. This makes it possible to grow a stoichiometric semiconductor material without requiring a degree of control over the beam fluxes and uniformity which would be impossible to achieve. For the group III materials, the sticking coefficient, the ratio of the atoms incorporated in the growth to those incident on the surface, is generally near unity, but re-evaporation must be taken into account at higher substrate temperatures.

2.2.1 MBE System

The MBE system used in our laboratory is a commercially manufactured Riber 2300 with 2" wafer capabilities. It consists of a load chamber, an analysis chamber and a growth chamber [19]. All of these are under ultra high vacuum (UHV), pumped with ion pumps. Recently a cryo-pump was added to the growth chamber to reduce the background pressure. Two of the chambers serve primarily as sample introduction chambers, or load locks, so that the integrity of the vacuum in the growth chamber is maintained. A cross section of the growth chamber is shown in Figure 2-2. During the growth, the pumping speed is increased by filling the cryo-panels with liquid nitrogen, and pressures in the 10^{-10} Torr range are achieved. The growth chamber is exposed to atmospheric pressure only when the material in the cells are depleted or a repair inside the chamber is needed. After each opening, several weeks of baking, degassing and calibration are required to grow crystals with a purity demanded by optoelectronic devices. The purpose of baking is to heat up the MBE system to a temperature high enough ($\approx 200°C$) that most gas molecules condensed during opening will outgas.

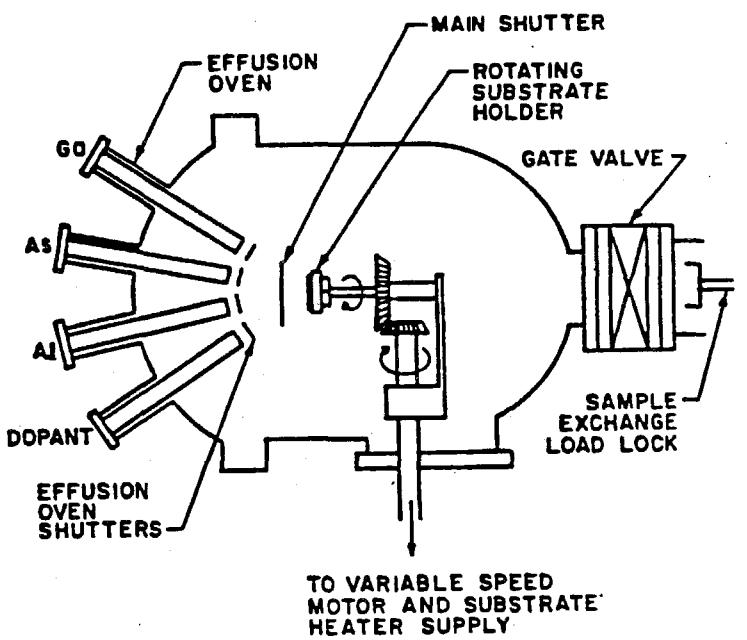

Figure 2-2: Deposition chamber, Riber 2300 molecular beam epitaxial system.

This is because the sticking coefficient of most molecules on the system walls changes by several orders of magnitude, in this range of temperature variation. During the baking the water vapor concentration in the chamber is monitored by a quadrupole mass spectrometer.

2.3 Sample preparation

The materials described in this thesis are known as III-Vs since they are comprised of elements from columns III and V of the periodic table. The epitaxial layers mainly consisted of $GaAs$, $AlGaAs$ and $InGaAs$. The nearly exact lattice parameter match between $GaAs$ (a=5.654$\AA$) and $AlAs$ (a=5.661$\AA$) permits the growth of closely matched heterostructures over the entire compositional range of $Al_xGa_{1-x}As$ with nearly ideal hyperabrupt interfaces.

The substrate which is a commercially available (100)-oriented $GaAs$ slice, is first cleaned in a boiling trichloroethylene (TCE), and then rinsed in acetone, methanol, and deionized water, to remove any wax or oil-based contamination on the wafer. After a wet chemical etching, the substrate is In-mounted to a Molybdenum block. As a result of these steps almost all of the carbon and other contaminations of the substrate are removed and a thin native oxide is left. This oxide layer protects the surface until it is introduced into the vacuum chamber.

2.4 Growth

In the loading chamber the sample is first heated to 250^oC, to remove any water vapor condensed on it, without affecting the wafer's protective oxide coating. Then the substrate is transferred to the analysis chamber where the pressure is about two orders of magnitude lower than that in the loading chamber. Finally the wafer is introduced into the growth chamber where a liquid nitrogen cooled shroud assures pressures in low 10^{-9} or 10^{-10} Torr range. These shrouds also attract excess material

which does not deposit on the substrate during the growth, preventing "memory effects" where a species from a previously grown layer can contaminate a present growth.

In the growth chamber the substrate is heated to $580°C$ over approximately five minutes, while the surface is monitored with the reflection high energy electron diffraction (RHEED) apparatus. As the substrate temperature approaches $580°C$, the protective oxide is desorbed. The RHEED pattern changes from a diffuse scattering off the disordered surface of the oxide, into the parallel lines generated by diffraction off the two-dimensional lattice of the crystal. When this pattern becomes sharp, an atomically clean surface is obtained and is ready for the growth.

2.4.1 RHEED pattern

RHEED uses a 8-15 KeV electron beam directed at a glancing angle ($\approx 1°$) to the substrate surface, and the diffracted beam is forward scattered and viewed on a phosphorous screen. The diffraction pattern from a crystal with a smooth surface is that of a two-dimensional surface due to the rapid attenuation of the beam in the crystal. The identification of the diffraction pattern requires knowledge of the surface reconstructions [8,19] . These rearrangements occur to minimize the surface free energy. The following notations are often used:

1. *GaAs* (100)-(m×n) means that a *GaAs* crystal is oriented with the (100) direction normal to the surface, and has a surface structure whose unit mesh is m×n times larger than the underlying bulk unit cell.

2. If the mesh is centered, the notation would be *GaAs* (100)-C(m×n).

In the case of *GaAs* (100) substrate there are two surface structures which are reported a Ga-stablized C(8×2) (or(4×2)) and an As-stablized C(2×8) (or(2×4)), see figures 2-3 and 2-4. Studying the interaction of Ga and As beams with *GaAs* surface, it was found that adsorption and desorption of Ga followed a simple first-order rate

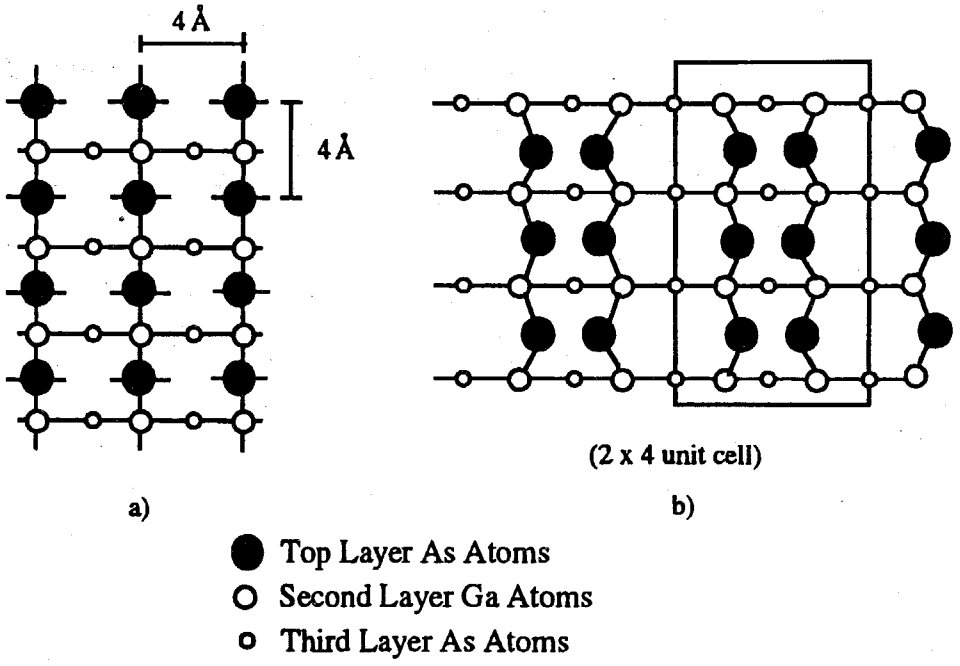

Figure 2-3: The structure (a) of the unreconstructed $GaAs$ (100) arsenic-rich surface. The missing dimer model (b) for the $GaAs$ (100) (2×4) surface[73].

equation and, in contrast, the behavior of arsenic was found to depend on the surface coverage of Ga. Therefore, stoichiometric $GaAs$ may be grown with the excess As flux being re-evaporated. Because of this, the substrate temperature and the flux ratio of incoming III/V materials are set so that As-stablized surface is maintained during the growth.

2.4.2 As_2 or As_4 fluxes?

Two types of arsenic sources are available. A typical Knudsen cell similar to the furnaces for the other sources may be used to supply tetrametric arsenic, As_4 which is the equilibrium vapor species over arsenic. However, the equilibrium vapor species over $GaAs$ is the As_2 dimer. Hence directly supplying As_2 is desirable. In our system the dimer arsenic is obtained using a 200cc Perkin-Elmer two-stage arsenic cracking

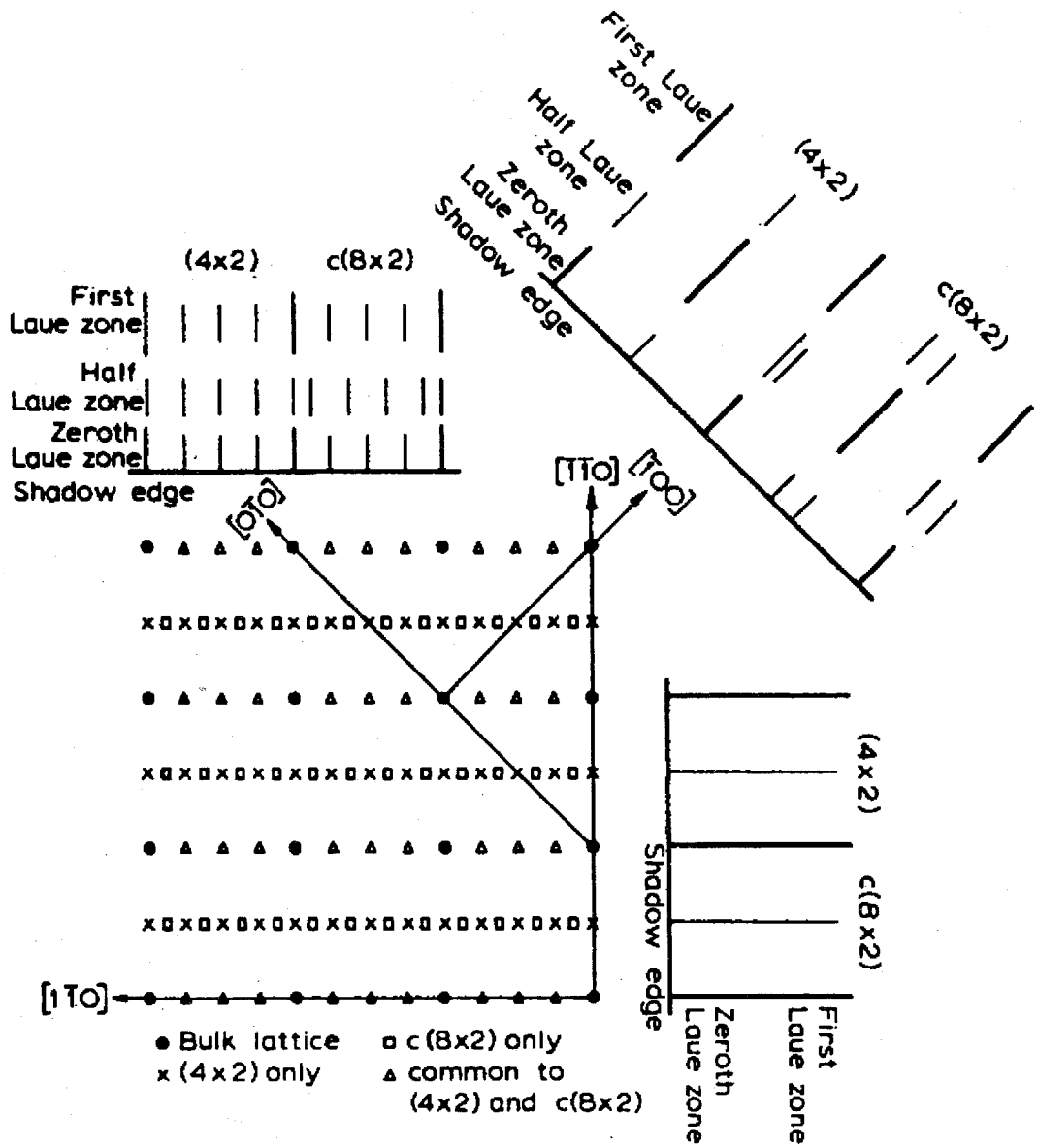

Figure 2-4: Reciprocal lattice section showing (4×2) and C(8×2) structures with the associated schematic RHEED pattern in different azimuths.

furnace or "cracker." A cracker consists of a low temperature sublimator section where solid arsenic is heated to control the magnitude of the flux, and a high temperature cracking section which produces As_2. It is believed that the incorporation of As_4 is a second order process whereby the As_4 molecule must first break into two As_2 dimers before incorporating on the surface. The sticking coefficient of As_4 is estimated to be ≤ 0.5 while that of As_2 is appreciably higher, approaching unity. Thus less As_2 than As_4 is required for successful growth. Studies have shown improved optical quality for material grown with As_2 [8]. High purity growth requires the minimum possible V/III ratios while maintaining an As-stablized condition.

2.5 Calibration

The oscillation of the RHEED intensity of the specular beam is related to the roughness of the growing surface. The MBE growth process is a layer-by-layer mode, with the individual layer starting at random nucleation sites that grow into islands and, finally, islands coalescing into a complete layer. The reflected beam intensity, therefore, has a maximum value at the completion of a monolayer (atomically smooth surface) and a minimum value at the half-monolayer point (atomically rough surface). The oscillations in the diffraction pattern from a growing surface, therefore, have a period corresponding to the growth of one monolayer. The intensity oscillation of the RHEED pattern is used to calibrate the $GaAs$ growth rate and the $AlAs$ mole fraction in $Al_xGa_{1-x}As$ to an unprecedented accuracy (see figure 2-5).

Further calibration of growth rates is done with flux measurement, using an ionization gauge which can be rotated into the path of the molecular beam (see figure 2-6). One notices a large transient overpressure, just after shutter opening. As discussed in the page 79 this transient was reduced by a 2' spacer between the cell and the MBE system.

After the growth, with the help of SEM, TEM and photoluminescence spec-

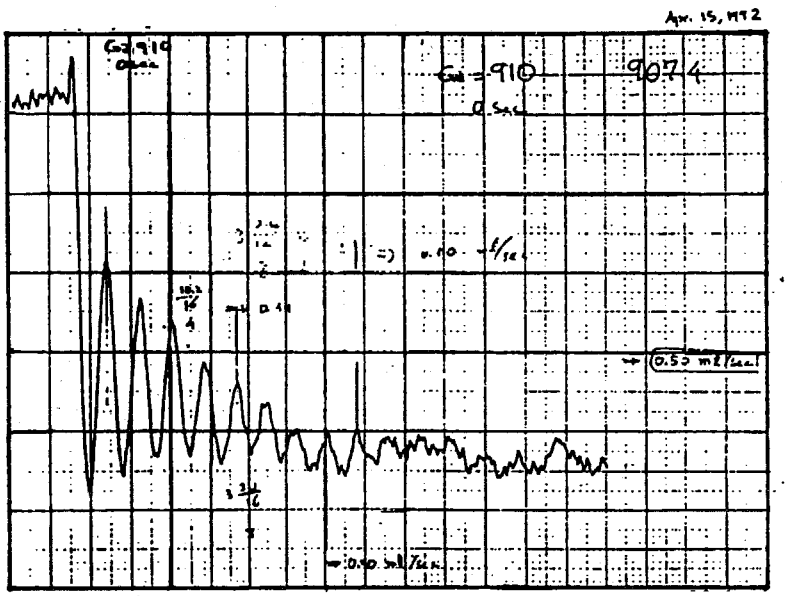

Figure 2-5: Typical intensity oscillations of the specular beam in the RHEED pattern. The period corresponds to the growth rate of a single $Ga + As$ layer.

troscopy, the thicknesses and compositions of the grown structures can be investigated. The concentration and the mobility of free carriers is measured using the Hall effect in a four-point Van der Paul geometry. The concentration of various contaminations in our MBE-grown samples was analyzed by secondary ion mass spectroscopy (SIMS) at Charles-Evans and Associates. Figure 2-7 shows that in the first samples grown after the opening of MBE (sample 1403), the background concentration of O and C was $1-2\times10^{18}$ and $4-5\times10^{15} atoms/cc$ respectively. After a year of growths (126 wafers), these contaminations were 5×10^{16} and $6\times10^{15} atoms/cc$.

With these high quality MBE-grown samples, the electron wave interference effects were observed over distances of the order of 40-50 nm [64,69]. These observations, based on the shape of the photocurrent spectrum and the sequential resonant tunneling induced negative differential resistance in the low temperature I-V characteristics, will be discussed in the future chapters.

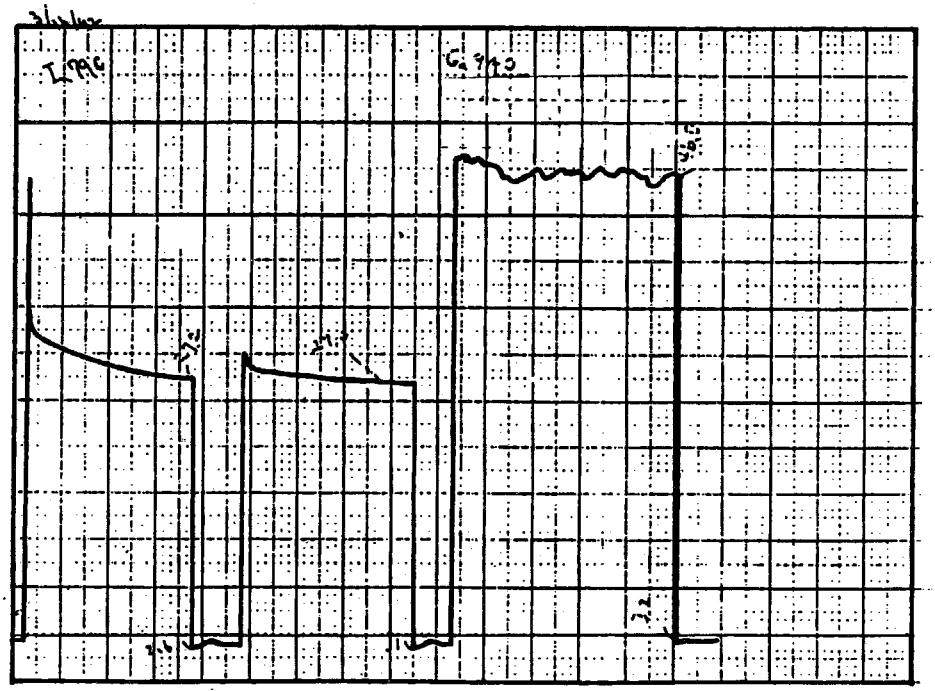

Figure 2-6: Flux of various materials arriving upon the substrate, measured with an ionization gauge. Note the transients after opening of the shutters

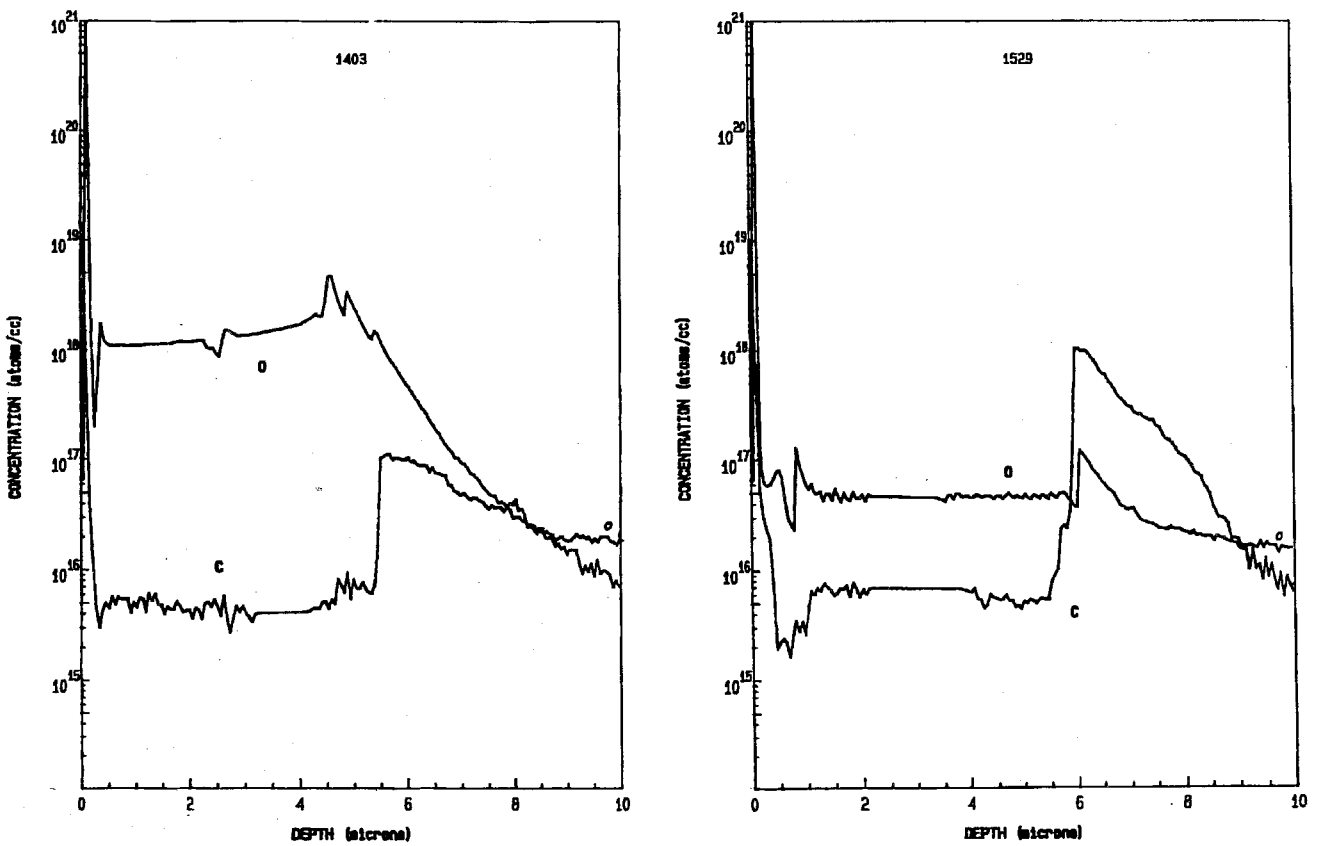

Figure 2-7: Secondary Ion Mass Spectroscopy of two MBE-grown wafers, showing the concentration of background impurities (C and O). The sample 1403 was grown after two weeks of baking and degassing following the opening of the MBE system to the atmospheric pressure. The sample 1529 was grown after 125 growths.

Chapter 3

Optical properties of quantum well intersubband transitions

In this chapter a description of the electronic states in the conduction band of $GaAs/AlGaAs$ multiquantum wells is presented using an envelope function approximation [1,2,7]. Deriving the wavefunctions and dipole matrix elements from the full multi-band Kane Hamiltonian, the controversial question of the strength of intersubband transitions versus interband transitions in quantum wells [28] is discussed. We will then study theoretically and experimentally, the absorption spectrum for transitions between energy levels inside a quantum well (i.e. bound-to-bound), and transitions between an energy level inside the quantum well and the states above the barrier (i.e. bound-to-continuum). For the latter case, the formation of minibands above the barrier, will modify the absorption lineshape. And finally, The effect of a DC electric field perpendicular to the MQW layers on the absorption spectrum is investigated. We will see that the experimental observations are well described by calculations based on the transfer matrix method, when the conduction band non-parabolicity and many-body effects are considered.

3.1 Electronic states in quantum wells

3.1.1 Band structure of the bulk GaAs

GaAs, like other III/V compounds, crystallizes in the zinc-blende structure. This lattice consists of two interpenetrating, face-centered cubic lattices, displaced from one another by a fourth of one of the cube main diagonals. There are 8 electrons per unit cell (3 from Ga and 5 from As) which contribute to the chemical bonds. Basically, orbitals of every atom (s-like or p-like) hybridize with an orbital of the neighboring atom, producing two levels, one bonding and one antibonding. Because there are a large number of unit cells, bonding and antibonding levels broaden into bands. The bonding s levels are strongly bound and always occupied by two electrons per unit cell. The remaining six electrons per unit cell completely fill the three bonding p orbitals (which form the *valance band*). The bands originating from the antibonding orbitals are all empty, the lowest lying (an s band) forms the *conduction band* of the material [2].

Electrons in the crystal obey the single-particle Schrödinger equation (neglecting many body effects):

$$\left[\frac{p^2}{2m_o} + V(\mathbf{r}) + \frac{\hbar}{4{m_o}^2c^2}(\sigma \times \nabla V).\mathbf{p}\right]\Psi(\mathbf{r}) = \varepsilon\Psi(\mathbf{r}), \tag{3.1}$$

where m_o is the free electron mass and $V(\mathbf{r})$ is the crystalline potential. The third term in Eq. 3.1 is the spin-orbit coupling (σ is the Pauli spin operator). This term results from the interaction energy of the electron's intrinsic magnetic moment with the magnetic field which appears in the electron frame when it is moving in an electrostatic potential ($V(\mathbf{r})$). The solutions to the Eq. 3.1 give the electronic stationary energies ε and wavefunctions $\Psi(\mathbf{r})$. Using the translational invariance of the crystalline potential, these solutions can be written in the Bloch form:

$$\Psi_{n\mathbf{k}}(\mathbf{r}) = Nu_{n\mathbf{k}}(\mathbf{r})exp(i\mathbf{k}.\mathbf{r}), \tag{3.2}$$

where N is a normalization coefficient and $u_{n\mathbf{k}}(\mathbf{r})$ a periodic function of $\mathbf{r}$ with the periodicity of the lattice. Various electronic eigenfunctions are labelled by two indices: a discrete one, n, which is called the band index; and a crystal wavevector $\mathbf{k}$, which can be restricted to the first Brillouin zone of the reciprocal lattice (the spin index is omitted for brevity). Substituting Eq. 3.2 in Eq. 3.1 gives

$$\left[\frac{p^2}{2m_o} + V(\mathbf{r}) + \frac{\hbar}{4{m_o}^2c^2}(\sigma \times \nabla V).\mathbf{p} + \frac{\hbar^2k^2}{2m_o} + \frac{\hbar\mathbf{k}}{m_o}\left(\mathbf{p} + \frac{\hbar}{4m_oc^2}\sigma \times \nabla V\right)\right] u_{n\mathbf{k}} = \varepsilon_{n\mathbf{k}} u_{n\mathbf{k}}. \tag{3.3}$$

k.p analysis

For many aspects of semiconductor electronic properties, the knowledge of the $\varepsilon_{n\mathbf{k}}$ relationship only over a small k range around the band extrema is needed, where the free carriers are located. One uses the fact that for any given $\mathbf{k}$, the set of all $u_{n\mathbf{k}}(\mathbf{r})$ ($n \in N$) is complete for functions having the periodicity of $V(\mathbf{r})$ [23,25]. Hence if we choose $\mathbf{k} = \mathbf{0}$, the Bloch function for any $\mathbf{k}$ may be expressed in terms of the Bloch function for $\mathbf{k} = \mathbf{0}$,

$$u_{n\mathbf{k}}(\mathbf{r}) = \sum_m c_{mn}(\mathbf{k}) u_{m\mathbf{0}}(\mathbf{r}). \tag{3.4}$$

This is called the **k=0** representation. Eq. 3.3 can be formally rewritten as:

$$[H(\mathbf{k} = \mathbf{0}) + W(\mathbf{k})]u_{n\mathbf{k}} = \varepsilon_{n\mathbf{k}} u_{n\mathbf{k}}, \tag{3.5}$$

where $H(\mathbf{k} = \mathbf{0})$ is the crystal Hamiltonian whose eigenfunctions are $\Psi_{n\mathbf{0}}$ (or $u_{n\mathbf{0}}$ equivalently):

$$H(\mathbf{k} = \mathbf{0})u_{n\mathbf{0}} = \varepsilon_{n\mathbf{0}} u_{n\mathbf{0}}. \tag{3.6}$$

One can easily convert Eq. 3.3 to a matrix eigenvalue equation by inserting Eq. 3.4 into Eq. 3.3, multiplying both sides of Eq. 3.3 by $u^*_{n\mathbf{0}}(\mathbf{r})$, and integrating over the unit cell in which the u's are normalized. Neglecting the spin-orbit term one gets:

$$\sum_m \left\{ \left(\varepsilon_{n\mathbf{0}} - \varepsilon_{n\mathbf{k}} + \frac{\hbar^2 k^2}{2m_o} \right) \delta_{nm} + \frac{\hbar \mathbf{k}}{m_o} . \langle n\mathbf{0}|\mathbf{p}|m\mathbf{0}\rangle \right\} c_{mn}(\mathbf{k}) = 0, \tag{3.7}$$

where:

$$\langle n\mathbf{0}|\mathbf{p}|m\mathbf{0}\rangle = \mathbf{p}_{nm} = \int_{unitcell} u^*_{n\mathbf{0}} \mathbf{p} u_{m\mathbf{0}} d^3\mathbf{r}. \tag{3.8}$$

In the equation 3.7, the explicit term due to the crystalline potential $V(\mathbf{r})$ is eliminated. So, one only (!) needs the $\mathbf{k} = \mathbf{0}$ Bloch state matrix elements ($\mathbf{p}_{nm}$) and energies ($\varepsilon_{n\mathbf{0}}$) to calculate the band structure for all other $\mathbf{k}$'s. But there is no direct way of measuring all of the Bloch state matrix elements. Eq. 3.7 is most useful when $\mathbf{k}$ is near $\mathbf{0}$ so that the nondiagonal part of the Hamiltonian can be treated as a perturbation. If all of the Bloch state matrix elements ($\mathbf{p}_{nm}$) vanished, we would recover the free electron dispersion relation for all of the bands: $\varepsilon_{n\mathbf{k}} = \varepsilon_{n\mathbf{0}} + \hbar^2 k^2 / 2m_o$. Thus, it is the presence of $\mathbf{p}_{nm}$ terms which determine the semiconductor electrical characteristics. There are two ways of treating the nondiagonal part of the Hamiltonian as a perturbation. One is through Löwdin's perturbation theory [46,23], which is presented in the next section. And the other one, proposed by Luttinger and Kohn [47], is by a canonical transformation of the basis in the form of $C = \exp(S)B$, S chosen such that the nondiagonal term of the Hamiltonian is removed. Through both of these methods, the removal of the nondiagonal $\mathbf{p}_{nm}$ term, will add a $\mathbf{k}$-dependent term to the diagonal part, which will modify the electronic dispersion relation. In the case of a single nondegenerate band, one finds:

$$\varepsilon_{n\mathbf{k}} = \varepsilon_{n\mathbf{0}} + \frac{\hbar^2 k^2}{2m_o} + \frac{\hbar^2}{m_o^2} \sum_{m \neq n} \frac{|\mathbf{p}_{nm}.\mathbf{k}|^2}{E_{n\mathbf{0}} - E_{m\mathbf{0}}}, \tag{3.9}$$

where the quadratic dependence on crystal momentum $\mathbf{k}$ can be interpreted as a

tensorial *effective* mass.

In the case of *GaAs* and *AlGaAs*, the accurate description of electronic states requires a nonperturbative treatment of coupling between several bands (conduction and valence), which is the subject of the next section.

Löwdin's perturbation theory

In ordinary perturbation theory an attempt is made to diagonalize the Hamiltonian h completely by an iterative process which works when all off-diagonal matrix elements h_{nm} are small compared to the unperturbed energy separations $(\varepsilon_n - \varepsilon_m)$ of the interacting levels. In Löwdin's method [46] one assumes that all states can be divided into two classes A and B. States in category A may interact strongly with one another but any state in category A interacts weakly with any state in category B. The interactions connecting states in A with states in B are then removed iteratively just as in ordinary perturbation theory, but no attempt is made in this first step to remove matrix elements connecting states in A. After removal of the interactions connecting A and B the states in A are left with "renormalized" interactions with one another. This "renormalized" interaction matrix must then be diagonalized exactly.

Use of symmetry

With the use of symmetries in the crystalline structure, one can chose a more convenient linear combination of Bloch states, to express the momentum matrix elements $\mathbf{p}_{mn}$ with minimum number of parameters. The irreducible representations of the point group at $\mathbf{k} = \mathbf{0}$ (the Γ point) [11,53], show that the valence band has the triply degenerate Γ_{15} representation, which corresponds to the bonding p-functions ($|x\rangle$, $|y\rangle$ and $|z\rangle$) in the tight-binding picture. The conduction band corresponding to antibonding $|s\rangle$-states, has the symmetry type Γ_1. Each of these states is twofold degenerate depending on electron spin. Because these bands are strongly coupled, it is appropriate to lump the conduction and valence bands together in Löwdin's

class A and put all other states in class B. In this case we will end up with an 8×8 Hamiltonian (4 bands, each twice degenerate due to spin). To further simplify the Hamiltonian, we will use the following linear combination of ($\mathbf{k}$=$\mathbf{0}$)-Bloch states, based on the total angular momentum $\mathbf{J}$ and its z-projection J_z:

$$\begin{aligned}
\text{(Conduction band) } u_{10} &= \left|S, \frac{1}{2}, \frac{1}{2}\right\rangle &&= i|S\uparrow\rangle \\
\text{(Heavy hole band) } u_{20} &= \left|P, \frac{3}{2}, \frac{3}{2}\right\rangle &&= \frac{1}{\sqrt{2}}|(X+iY)\uparrow\rangle \\
\text{(Light hole band) } u_{30} &= \left|P, \frac{3}{2}, \frac{1}{2}\right\rangle &&= -\sqrt{\frac{2}{3}}|Z\uparrow\rangle + \frac{1}{\sqrt{6}}|(X+iY)\downarrow\rangle \\
\text{(Split}-\text{off band) } u_{40} &= \left|P, \frac{1}{2}, \frac{1}{2}\right\rangle &&= \frac{1}{\sqrt{3}}|(X+iY)\downarrow\rangle + \frac{1}{\sqrt{3}}|Z\uparrow\rangle,
\end{aligned} \tag{3.10}$$

and similarly for 4 other bands: $|S,1/2,-1/2\rangle$, $|P,3/2,-3/2\rangle$, $|P,3/2,-1/2\rangle$, $|P,1/2,-1/2\rangle$. Assuming $\mathbf{k}_\perp = \mathbf{0}$ (for example in the $x-y$ plane), the matrix equation 3.7 will be reduced to the following 3×3 form:

$$\begin{pmatrix}
E_c - E_c(k_z) + \frac{\hbar^2 k_z^2}{2m_o} & \sqrt{\frac{2}{3}}\frac{p_{cv}}{m_o}\hbar k_z & -\sqrt{\frac{1}{3}}\frac{p_{cv}}{m_o}\hbar k_z \\
\sqrt{\frac{2}{3}}\frac{p_{cv}}{m_o}\hbar k_z & E_{lh} - E_{lh}(k_z) + \frac{\hbar^2 k_z^2}{2m_o} & 0 \\
-\sqrt{\frac{1}{3}}\frac{p_{cv}}{m_o}\hbar k_z & 0 & E_{so} - E_{so}(k_z) + \frac{\hbar^2 k_z^2}{2m_o}
\end{pmatrix} \times$$
$$\begin{pmatrix}
c_{c,c}(k_z) & c_{c,lh}(k_z) & c_{c,so}(k_z) \\
c_{lh,c}(k_z) & c_{lh,lh}(k_z) & c_{lh,so}(k_z) \\
c_{so,c}(k_z) & c_{so,lh}(k_z) & c_{so,so}(k_z)
\end{pmatrix} = \begin{pmatrix} 0 \\ 0 \\ 0 \end{pmatrix}, \tag{3.11}$$

where c, lh, and so label conduction, light-hole and, split-off bands, respectively. The momentum matrix element p_{cv} between bulk Bloch states can also be written as $p_{cv} = i\sqrt{m_o E_p/2}$, where E_p is the Kane energy ($\sim 20eV$ in III-V semiconductors). In the Hamiltonian matrix the non-diagonal terms ($\propto k_z$) represent the direct coupling between conduction and valence bands. To take into account the coupling to the other

bands à la Löwdin, the following matrix should be added to the 3×3 Hamiltonian:

$$\begin{pmatrix} (\frac{1}{2m'} - \frac{1}{2m_o})\hbar^2 k_z^2 & 0 & 0 \\ 0 & (\frac{-\gamma_1 - 2\gamma_2}{2m_o} - \frac{1}{2m_o})\hbar^2 k_z^2 & \frac{\sqrt{2}}{m_o}\gamma_2 \hbar^2 k_z^2 \\ 0 & \frac{\sqrt{2}}{m_o}\gamma_2 \hbar^2 k_z^2 & (\frac{-\gamma_1}{m_o} - \frac{1}{2m_o})\hbar^2 k_z^2, \end{pmatrix} \tag{3.12}$$

where, m' (conduction band effective mass due to *remote bands*), γ_1, and γ_2 (the Luttinger parameters [2]) can be expressed using the momentum matrix elements, and the band-edge energies. For example, from an equation similar to 3.9 one gets:

$$\frac{1}{2m'} = \frac{1}{m_o^2} \sum_j^{\Gamma_{15},\Gamma_{25'}} \frac{|\langle s|p_x|u_j \mathbf{0}\rangle|^2}{E_c - E_j}. \tag{3.13}$$

It is interesting that Luttinger [48], derived the minimum parameters needed to describe a quadratic band structure, based solely on symmetry arguments, without calculating the $k.p$ perturbation series. These parameters are actually determined experimentally, and are given for various semiconductor compounds.

Solving the matrix eigenvalue equation 3.11, one gets the bulk band structure (i.e. the dispersion relations: $E_c(k_z)$, $E_{lh}(k_z)$, and $E_{so}(k_z)$, and in the same way $E_n(\mathbf{k})$ for other bands or k-space directions).

To see how we can apply the results of the previous section to the case of heterostructures (made of layers of different semiconductors), we will first briefly review the effective-mass equation.

3.1.2 The effective mass equation

We consider the motion of an electron in a semiconductor in the presence of some additional *slowly varying* and *weak* potential $U(\mathbf{r})$. We will follow the derivation of Luttinger and Kohn [47] (this problem is also known as the treatment of shallow impurity states in semiconductors [30]). The solution to the Schrödinger equation (neglecting spin-orbit term):

$$\left[\frac{p^2}{2m_o} + V(\mathbf{r}) + U(\mathbf{r})\right]\psi(\mathbf{r}) = E\psi(\mathbf{r}), \tag{3.14}$$

can be written as a linear combination of the solutions without the perturbation, which was given in the equation 3.2. For example using (**k**=**0**)-Bloch states, we get:

$$\psi(\mathbf{r}) = \sum_{\text{bands: } n=1}^{8} c_n f_n(\mathbf{r}) u_{n\mathbf{0}}(\mathbf{r}), \tag{3.15}$$

where the $f_n(\mathbf{r})$'s are *envelope functions* which vary slowly over the scale of a unit cell in the crystal, and where the $u_{n\mathbf{0}}(\mathbf{r})$'s are the Γ-point Bloch functions for the conduction and valence bands (8 bands). For instance, if $U(\mathbf{r})$ vanishes, the f_n are the plane waves $Nexp(\mathbf{k}.\mathbf{r})$.

By inserting equation 3.15 into equation 3.14, multiplying by $u^*_{m\mathbf{0}} f^*_m$ and integrating over the crystal volume we obtain an eigenvalue matrix equation for the coefficients $c_n f_n(\mathbf{r})$. Using the fact that there are two scales in the problem, one representing the variations over unit cells ($u_{m\mathbf{0}}$), and the other one varying very slowly over the unit cell (f_m); the eigenvalue equation is further simplified, and it can be formally rewritten as:

$$\sum_{n=1}^{8} \left[H_{mn}(-i\nabla) + U(\mathbf{r})\delta_{mn}\right] f_n(\mathbf{r}) = E f_m(\mathbf{r}), \tag{3.16}$$

where $H_{mn}(-i\nabla)$ is the (8×8) **k.p** Hamiltonian (a simplified 3×3 version was given in the equation [3.11] + [3.12]), in which the momentum **k** is replaced by the differential operator $-i\nabla$. This is a very important result, revealing that in presence of a slowly varying and weak potential, one does not need to directly solve the Schrödinger equation with the crystalline potential term. Instead, one can use an *effective* Schrödinger equation in which the influence of the underlying crystalline structure is represented through some *effective* parameters (m^*,γ_1,γ_2,γ_3, etc.). This result is a direct consequence of the slow variation of envelope functions over the unit cell. In the case of superlattices and quantum wells the additional potential term

in the Schrödinger equation is not slowly varying anymore, but the fact that the electronic wavefunctions are still smoothly varying is an indication of the possibility of using the effective mass equation, when care is taken for the boundary conditions (see section 3.1.3).

Electronic wavefunctions for the effective mass equation

Solving the effective mass equation 3.16, one gets the electronic state eigen-energies (E) and the associated envelope functions (f_n). The total electronic eigenfunction is given by the equation 3.15:

$$\psi(\mathbf{r}) = \sum_{\text{bands: } n=1}^{8} c_n f_n(\mathbf{r}) u_{n\mathbf{0}}(\mathbf{r}). \tag{3.17}$$

It is important to note that rigorously, the summation in this equation should run over all of the bands $n = 1, \cdots, \infty$. When one uses only a limited number of them (e.g. 8) and considers the interaction with the remote bands through Löwdin's method; not only the Hamiltonian matrix elements are "renormalized" but also the band edge Bloch states [1]:

$$\tilde{u}_{n\mathbf{0}}(\mathbf{r}, \mathbf{k}) = u_{n\mathbf{0}}(\mathbf{r}) + \sum_{m>8} \frac{\mathbf{k}.\mathbf{p}_{mn}}{m_o(\varepsilon_{n\mathbf{0}} - \varepsilon_{m\mathbf{0}})} u_{m\mathbf{0}}(\mathbf{r}). \tag{3.18}$$

The linear term in $\mathbf{k}$, gives an additional term to the total wavefunction, which can be written as:

$$\psi(\mathbf{r}) = \sum_{\text{bands: } n=1}^{8} c_n \left[f_n(\mathbf{r}) u_{n\mathbf{0}}(\mathbf{r}) + \sum_{m>8} \frac{-i(\nabla f_n(\mathbf{r})).\mathbf{p}_{nm}}{m_o(\varepsilon_{n\mathbf{0}} - \varepsilon_{m\mathbf{0}})} u_{m\mathbf{0}}(\mathbf{r}) \right]. \tag{3.19}$$

Equation 3.19 shows that to the lowest order, the electronic wavefunction is a sum of the conduction and valence band Bloch states times the associated envelope functions. The correction term is due to the contribution of other bands ($\mathbf{k} = \mathbf{0}$)

Bloch states, and is proportional to the *gradient* of the envelope functions.

3.1.3 Band structure of $GaAs/AlGaAs$ quantum wells

To find the electronic structure of quantum well devices, we need to find out how the above bulk-like envelope functions are connected at the boundaries between different semiconductor layers. The boundary condition for an electron at a potential barrier is normally simply taken to be continuity of the wavefunction and its derivative normal to the boundary. This is a direct result of first and second integrations of the Schrödinger equation across the boundary. This is not valid for envelope functions, because they are not the full wavefunctions. In the following section, based on the effective mass equation, the boundary conditions for the envelope functions are derived.

Boundary conditions

Heterojunctions, quantum wells and superlattices are made of several layers of different semiconductor materials. Each layer has its own band structure parameters (m^*, E_c, E_{lh}, E_{so}, etc.). One could think of writing a more general form of equation 3.16, in which the effective masses and the band edges vary as a function of z (the growth direction). For example the conduction band envelope function equation (scalar version of the equation 3.16) could be written as:

$$\left[-\frac{\hbar^2}{2}\nabla.\left(\frac{1}{m^*(z)}\nabla\right)+U(\mathbf{r})+E_c(z)\right]f_c(\mathbf{r})=Ef_c(\mathbf{r}). \tag{3.20}$$

The kinetic energy term has been rewritten, for a z-dependent mass, in a way which restores the hermitian character of the Hamiltonian. But we can not take this equation seriously, because the variations in $m^*(z)$ and $E_c(z)$, takes place over a few lattice distances. These variations are too fast for the effective mass formalism to be valid. Nevertheless, we can learn something about the boundary conditions from

this differential equation. Integrating equation 3.20 between infinitesimal distances $z = -\epsilon$ (on one side of the heterojunction in the material A) and $z = +\epsilon$ (on the other side of the heterojunction in the material B), we obtain:

$$\begin{aligned} f_c^A(-\epsilon) &= f_c^B(+\epsilon) \\ \frac{1}{m_A^*}\left(\frac{\partial}{\partial z} f_c^A\right)_{-\epsilon} &= \frac{1}{m_B^*}\left(\frac{\partial}{\partial z} f_c^B\right)_{+\epsilon} . \end{aligned} \tag{3.21}$$

In order for the boundary conditions 3.21 on the envelope functions to make physical sense, we must see their implication on the total wavefunction as described by the scalar version of the equation 3.19. In order for ψ to be continuous when f_c is, one must assume $u_{c\mathbf{0}}^A \simeq u_{c\mathbf{0}}^B$ and that the second term of the wavefunction in the equation 3.19 be small, i.e. that the $\mathbf{k}$-dependence of the Bloch function $u_{c\mathbf{k}}$ about $\mathbf{k} = \mathbf{0}$ be weak. The former assumption is plausible in the III-V semiconductor family, as long as we are considering the same band edges on both side of heterojunctions (e.g. the conduction band direct minimum).

One can also show that the above mentioned boundary conditions, assure the conservation of the probability current, and ultimately the stationarity of the heterostructure wavefunction.

Conduction band energy levels in quantum wells and superlattices, non-parabolic effects

Based on the arguments of the previous section, to calculate the energy levels and wavefunctions of a $GaAs/AlGaAs$ multiquantum well structure, we can use the **k.p** Hamiltonian. Taking the growth direction as z, and assuming the in-plane momentum to vanish, the 8×8 Hamiltonian is reduced to a 3×3 one. We thus get the following equation for the envelope functions:

$$\begin{pmatrix} E_c(z) & \sqrt{\frac{2}{3}}\frac{p_{cv}}{m_o}p_z & -\sqrt{\frac{1}{3}}\frac{p_{cv}}{m_o}p_z \\ -\sqrt{\frac{2}{3}}\frac{p_{cv}}{m_o}p_z & E_{lh}(z) & 0 \\ \sqrt{\frac{1}{3}}\frac{p_{cv}}{m_o}p_z & 0 & E_{so}(z) \end{pmatrix} \begin{pmatrix} f_c(z) \\ f_{lh}(z) \\ f_{so}(z) \end{pmatrix} = E \begin{pmatrix} f_c(z) \\ f_{lh}(z) \\ f_{so}(z) \end{pmatrix}. \tag{3.22}$$

This (3×3) Hamiltonian is deduced from the equation 3.11, replacing p_z with the operator $-i\hbar\partial/\partial z$, ignoring the contribution of the remote bands (i.e. equation 3.12), and also neglecting the diagonal "free electron" term $p_z^2/2m_o$, which can be shown to only contribute terms of order $(E_c - E_{lh,so})/E_p << 1$ (we saw that $p_{cv} = i\sqrt{m_o E_p/2}$, and $E_p \sim 20eV$). The total electronic wavefunction, in the lowest order approximation, can be written as:

$$\psi(\mathbf{r}) = f_c(z)u_{c,\mathbf{0}}(\mathbf{r}) + f_{lh}(z)u_{lh,\mathbf{0}}(\mathbf{r}) + f_{so}(z)u_{so,\mathbf{0}}(\mathbf{r}). \tag{3.23}$$

Now, as we are only interested in the energy levels located above the edge of the conduction band, the problem can be solved using the second and third rows of 3.22 to express the equation in the first row as

$$p_z \frac{1}{2m(E,z)} p_z f_c + E_c(z) f_c = E f_c, \tag{3.24}$$

with the energy- and position-dependent effective mass

$$\frac{1}{m(E,z)} = \frac{1}{m_0}\left[\frac{2}{3}\frac{E_p}{E - E_{lh}(z)} + \frac{1}{3}\frac{E_p}{E - E_{so}(z)}\right]. \tag{3.25}$$

This energy-dependent effective mass represents the deviation of electronic dispersion relationship from the k^2-law (free electron type) behavior, so it is often refered to as *nonparabolicity*.

The solutions of the differential equation 3.24 give the conduction component and the energy of the stationary states. However the total stationary wavefunction is given by the three components f_c, f_{lh}, and f_{so}, weighted with their corresponding Bloch

functions, so that the only knowledge of the conduction component is, in principle, insufficient for the complete physical description of the stationary state. One should use the solution of equation 3.24, to derive the light-hole and split-off components from equation 3.22.

To solve the Schrödinger equation 3.24 for a multiquantum well device, the structure is divided into a series of bulk-like regions. In each region the effective mass $m(E)$ and the band edge E_c are position independent, so the equation 3.24 is reduced to a second-order differential equation with constant coefficients. The solution to the equation in each region is a combination of two plane waves, one right-going, and the other one left-going. Writing the appropriate boundary conditions at the interface between two semiconductors(equation 3.21), we end up with a matrix equation relating the coefficients of right- and left-going waves on both sides of the interface. Multiplying these matrices from one side of the device to the other side, and imposing the "physical" boundary conditions at the edges, we will get a nonlinear eigenvalue equation for the energy E, the corresponding eigen-functions f_c are the conduction-band envelope-function stationary states. This so called "Transfer matrix method" was implemented by Yuanjian Xu, and was used to calculate electrical and optical properties of our MBE-grown devices.

3.1.4 Coulomb and exchange interactions, self-consistent calculations

Using the transitions between energy levels in the conduction band for infrared detector applications requires a high doping density, so the Coulomb interaction may lead to a substantial modification of the band structure. This was taken into account by solving the one-dimensional Poisson equation:

$$\frac{d}{dz}\left(\epsilon(z)\frac{dV_C}{dz}\right) = \frac{e}{\epsilon_o}\left(N_D^+(z) - n(z)\right), \tag{3.26}$$

self-consistently with the Schrödinger equation. Here, $\epsilon(z)$ is the bulk material's static dielectric function, $N_D^+(z)$ doping density, $n(z)$ the electronic charge density, and V_C the Coulomb potential. Furthermore, at these high densities the many-body effects become important. This was taken into account by an additional term in the Hamiltonian (exchange-correlation potential energy):

$$V_{xc}(r_s) = -\left(\frac{9\pi}{4}\right)^{1/3}\left(1+0.7734\frac{r_s}{21}\ln\left(1+\frac{21}{r_s}\right)\right)\frac{2R_y^*}{\pi r_s}, \tag{3.27}$$

where the Rydberg energy, $R_y^* \equiv e^2/8\pi\epsilon_s\epsilon_o d_o$, $d_o$is the semiconductor Bohr radius, and the density parameter is given as: $r_s \equiv (3/4\pi a_o^3 n(z))^{1/3}$.

3.2 Optical transitions

Optical transitions between stationary states of a system are commonly described in terms of oscillator strengths f, defined as

$$f_{ij} = \frac{2}{m_o}\frac{|\langle\psi^{(i)}|\mathcal{P}|\psi^{(j)}\rangle|^2}{E_i - E_j}, \tag{3.28}$$

where $\psi^{(i)}$ and $\psi^{(j)}$ are stationary states and $\mathcal{P}$ is the momentum operator. In the matrix notation adopted in the preceding section, the momentum operator corresponding to the Hamiltonian 3.22 is given by [2]:

$$\mathcal{P} = \begin{pmatrix} 0 & \sqrt{\frac{2}{3}}p_{cv} & -\sqrt{\frac{1}{3}}p_{cv} \\ -\sqrt{\frac{2}{3}}p_{cv} & 0 & 0 \\ \sqrt{\frac{1}{3}}p_{cv} & 0 & 0 \end{pmatrix}. \tag{3.29}$$

In order to be consistent with Hamiltonian 3.22, where the free-electron term was neglected, we have dropped the diagonal p_z term in the momentum matrix. One can show that the momentum matrix element in 3.28 is simply related to the conduction components of the total wavefunction as

$$\langle\psi^{(i)}|\mathcal{P}|\psi^{(j)}\rangle = \frac{1}{2}\left\langle f_c^i \left| p_z \frac{m_o}{m(E_i,z)} + \frac{m_o}{m(E_j,z)} p_z \right| f_c^j \right\rangle, \tag{3.30}$$

with $m(E)$ given by 3.25. It is interesting to note that if the z-dependence of effective mass is ignored, the equation for oscillator strength 3.28 becomes:

$$f_{ij} \simeq \frac{2}{m(E)} \frac{|\langle f^{(i)}|p_z|f^{(j)}\rangle|^2}{E_i - E_j}. \tag{3.31}$$

The interpretation of this equation is as follows: when an electron of mass m_o is excited by photons from the *stationary* state $|\psi^{(i)}>$ to the *stationary* state $|\psi^{(j)}>$, it can be viewed as an "envelope" electron of effective mass $m(E)$ making transitions between *envelope* states $|f^{(i)}>$ and $|f^{(j)}>$. Or alternatively, the envelope electron is "dressed" through its interactions with various other bands, by an *effective* mass.

3.2.1 Strengths of intersubband transitions versus interband transitions

Single-band analysis

INTERBAND TRANSITIONS The transition probability between quantum well states due to an incident radiation is given by Fermi's golden rule, and it is the product of an optical matrix element times a density of states. In the dipole approximation the interaction Hamiltonian is -er.E, and the optical matrix element (M) has the form:

$$M \propto |\langle e|\mathbf{r}.\eta|h\rangle| = \int f_e(z) e^{i\mathbf{k}_{e,\perp}.\mathbf{r}_\perp} u_{e,\mathbf{k}_e}(\mathbf{r}) \eta.\mathbf{r} f_h(z) e^{i\mathbf{k}_{h,\perp}.\mathbf{r}_\perp} u_{h,\mathbf{k}_h}(\mathbf{r}) d\mathbf{r}, \tag{3.32}$$

where $|h\rangle$ and $|e\rangle$ are initial and final transition states, f_h, f_e the envelope wave functions, $\mathbf{k}_h$, $\mathbf{k}_e$ are the wavevectors, η the polarization vector of light, $u_{h\mathbf{k}_h}(\mathbf{r})$ and $u_{e\mathbf{k}_e}(\mathbf{r})$ are the usual Bloch functions. The integral contains fast-varying functions over unit cells (u's) and slowly varying functions (f's). One transforms equation 3.32

in a summation of localized integrals involving only Bloch functions over the N crystal unit cells labeled by their centers $\mathbf{R}_j$:

$$M \simeq \sum_{\mathbf{R}_j} f_h(\mathbf{R}_j) f_e(\mathbf{R}_j) e^{i(\mathbf{k}_{h,\perp} - \mathbf{k}_{e,\perp}).\mathbf{R}_j} \int_{cell} u_{h,\mathbf{k}_h}(\mathbf{r}) \eta.\mathbf{r} u_{e,\mathbf{k}_e}(\mathbf{r}) d\mathbf{r}. \tag{3.33}$$

The latter integral is independent of $\mathbf{R}_j$ and is ΩP where Ω is the unit cell volume and P the usual 3D matrix element that contains the selection rules due to the band symmetries and light polarization. When summing for the transverse directions, exponential factor gives a null contribution unless $\mathbf{k_{h,\perp}} = \mathbf{k_{e,\perp}}$, which is the vertical transition selection rule. The only difference between equation 3.33 and the usual 3D summation lies in the z-direction summation, which produces a factor $\sum f_e(\mathbf{R}_j) f_h(\mathbf{R}_j) a$, where the $\mathbf{R}_j$'s are the lattice cell centers in the z direction and a is the lattice constant.

Transforming back into an integral, $\int f_e(z) f_h(z) dz$, one finds a unity factor for the transitions between electron and hole states with the same quantum number n, as the f's are identical ($\sim \sin(n\pi z/L)$) and normalized to unity. The optical matrix element is therefore the same in 2D and 3D. In the abscence of excitonic effects, the absorption coefficient should reflect the reduced 2D density-of-states.

INTERSUBBAND TRANSITIONS The optical matrix element M takes a much different shape when dealing with intersubband transitions, i.e. between confined electron states or hole states only. In this case, the fast-varying integrals involve the same periodic part of the wavefunction, which then have zero matrix element with $\mathbf{r}$. We will then have:

$$M \sim \int_{crystal} f_e^{(1)}(z) \eta.\mathbf{r} f_e^{(2)}(z) dr \int_{cell} u_{e\mathbf{k}_e}(\mathbf{r}) u^*_{e\mathbf{k}_e}(\mathbf{r}) d^3\mathbf{r}. \tag{3.34}$$

The second integral yields unity when using normalized Bloch functions. The matrix element now has large values, of the order of L, dimension of the quantum

well, instead of an atomic dimension, as in interband transitions. This is what is known as the "giant" dipole effect.

Multi-band analysis

Based on the analysis of the previous section, one is tempted to say that the strength of the intersubband transitions is much larger than the interband ones. But in reality, we should compare the oscillator strength of these two transitions:

$$f \equiv 2\frac{|\langle f|\eta.\mathbf{p}|i\rangle|^2}{m\hbar\omega} = \frac{2m\omega}{\hbar}|\langle f|\eta.\mathbf{r}|i\rangle|^2. \tag{3.35}$$

It is true that for the usual material parameters of $GaAs/AlGaAs$ quantum wells, the dipole matrix element of intersubband transitions is larger than the interband one, but for the same material parameters, the intersubband energies are smaller than the interband ones. So the two effects might cancel each other in the equation for oscillator strength. In, fact using the infinite well approximation, Khurgin proved [28] that:

$$\frac{|\langle h|\eta.\mathbf{p}|e\rangle|^2}{m\hbar\omega_{eh}} \simeq \frac{|\langle e,1|\eta.\mathbf{p}|e,2\rangle|^2}{m\hbar\omega_{12}}. \tag{3.36}$$

But in Khurgin's analysis (equation (10) in his paper), the masses in the oscillator strength equation 3.35 are assumed to be free electron mass (m_o), for both interband and intersubband transitions. Through the derivation of the equation 3.31, we saw that for intersubband transitions one should use the *effective* mass for oscillator strength [2]. A similar multi-band analysis for interband transitions can show that the correct mass to use is the *free* electron mass.

So, in fact the intersubband transitions have a larger oscillator strength than the interband ones. This is because the conduction band electrons are "lighter" (through interactions with other bands), and not inherently for the spatial extent of envelope functions.

3.2.2 Absorption spectrum of bound-to-bound and bound-to-continuum transitions

In the case of bound-to-bound QWIPs, the absorption spectrum is a Lorentzian shape peak corresponding to a transition between the ground state and the first excited state. The contribution of other states in the continuum above the barrier is negligible because of the oscillator strength sum rule (one-to-two transition, both states being localized in the well, has the most significant dipole matrix element). Figure 3-1 shows the experimental absorption spectrum of a sample of thirty periods of 7nm $GaAs$ quantum wells, separated by 44nm $Al_{0.3}Ga_{0.7}As$ barriers. The quantum wells were doped with Silicon to $2 \times 10^{18} cm^{-3}$. The absorption spectrum of a $2.6mm$ long sample, cleaved and lapped to 45^{o} angled facets on both ends, was measured by Gilad Almogy, with a Fourier transform infrared spectrometer. One can see excellent Lorentzian curve fits at $77K$ and $300K$, showing a homogeneous broadening.

When the quantum well parameters allow only one state in the well (i.e. a bound-to-continuum QWIP), the absorption spectrum is not Lorentzian any more, several states above the barriers have a strong contribution to the absorption. At zero bias, due to the translational symmetry of the potential there are well known minibands in the continuum states of the superlattice. Figure 3-2 shows the experimental and the theoretical absorption spectrum at a temperature of $80K$, for a sample consisting of 50 periods of 4nm $GaAs$ wells, uniformly doped with Si to $n = 2 \times 10^{18} cm^{-3}$, separated by 20nm $Al_{0.22}Ga_{0.78}As$ barriers [69]. One notices an excellent fit with the calculations which included exchange-correlation potential and energy dependent effective mass. The shallow satellite peaks correspond to the position of miniband in the continuum states.

Under an applied bias, such that the voltage drop per period is bigger than the miniband gaps, the miniband structure is destroyed. But the theoretical calculations (see figure 3-3), and the experimental photocurrent spectrum at low temperatures (see figure 3-4) show that the satellite peaks in the spectrum are becoming more

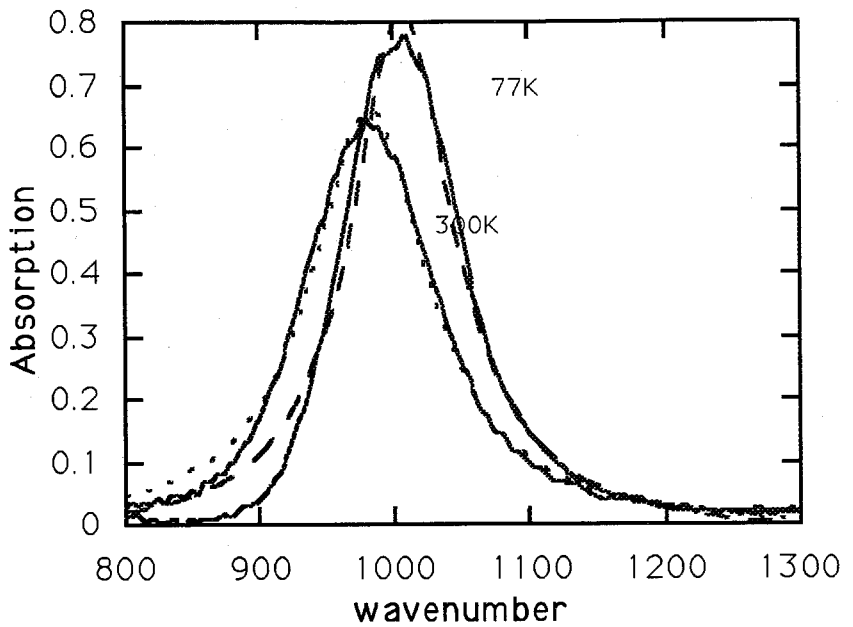

Figure 3-1: Absorption spectrum of bound-to-bound transitions in a multiquantum well device at $77K$ and $300K$. The dashed lines are Lorentzian curve fits.

pronounced. The physical origin of these observed peaks is that the dipole matrix element which is basically an overlap integral between the *localized* ground state in the well and the excited states above the barrier, is sensitive to the *local* density-of-states (i.e. density-of-states normalized by the amplitude of the wavefunction in the well region), and it reflects the electron interferences over neighboring wells [69]. Whereas the total density-of-states, which shows the energy level spacing for the whole superlattice, does not have any noticeable structure.

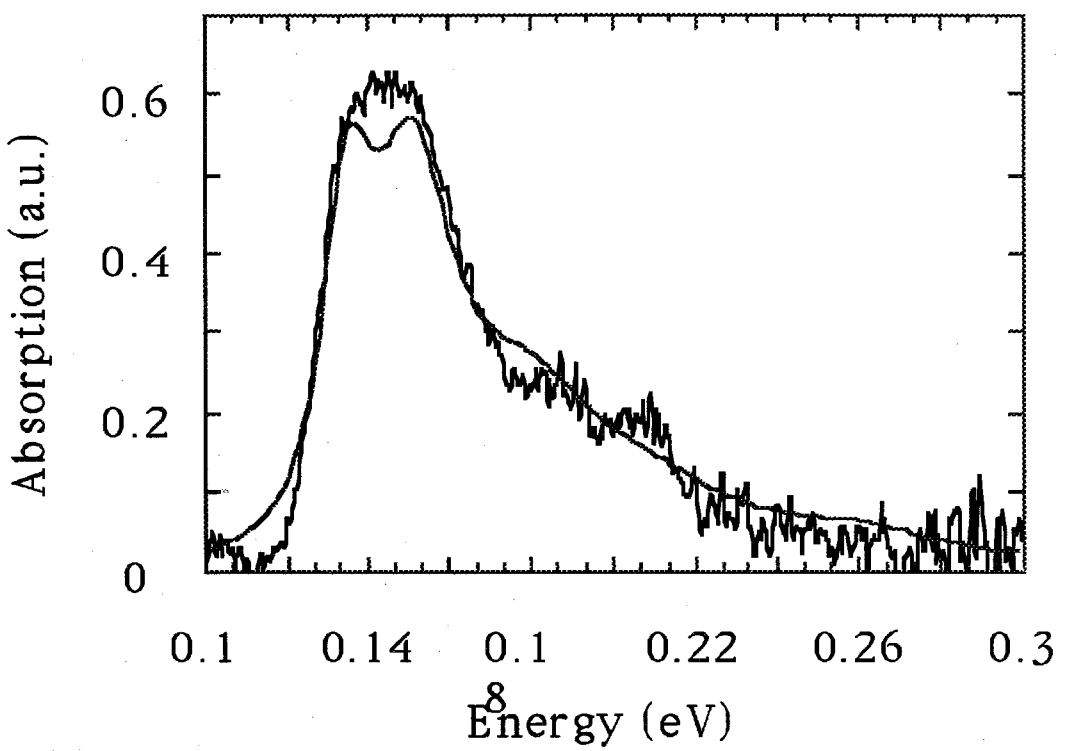

Figure 3-2: Theoretical and experimental absorption spectrum of a bound-to-continuum quantum well infrared photodetector

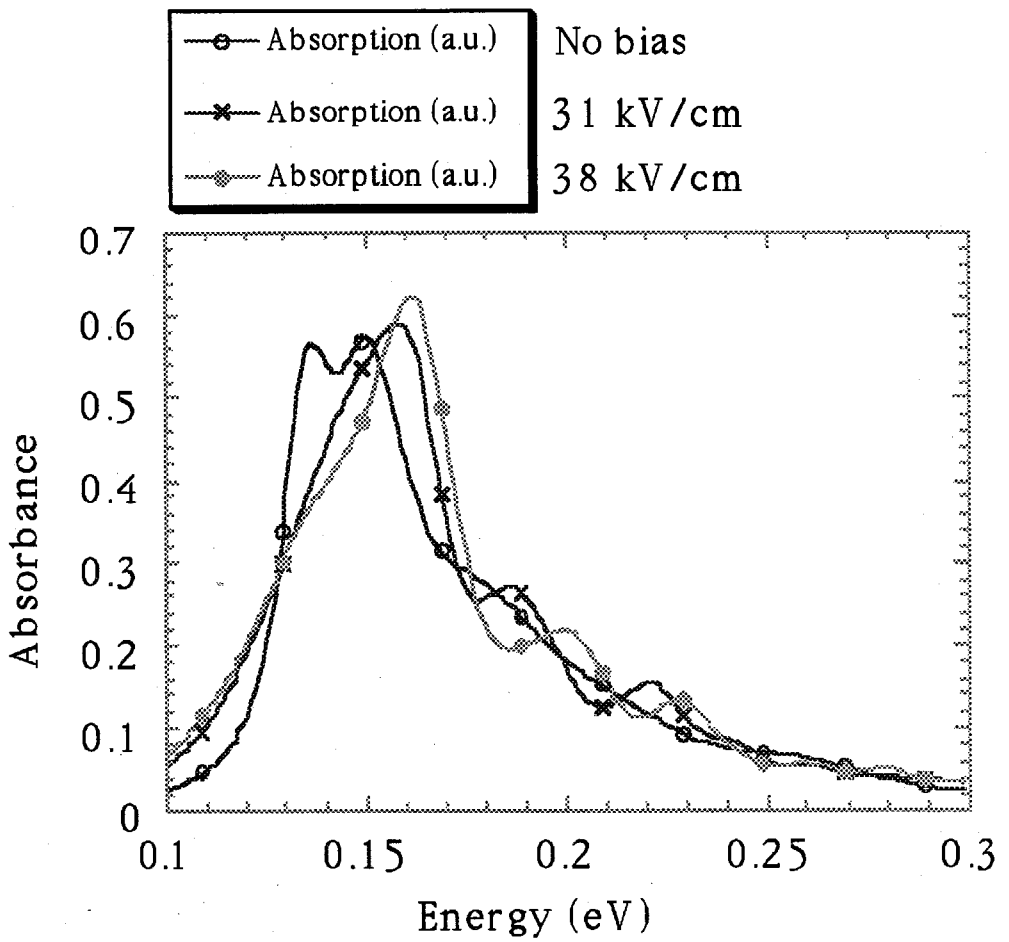

Figure 3-3: Theoretical absorption spectrum of a bound-to-continuum quantum well infrared photodetector, calculated for different biases

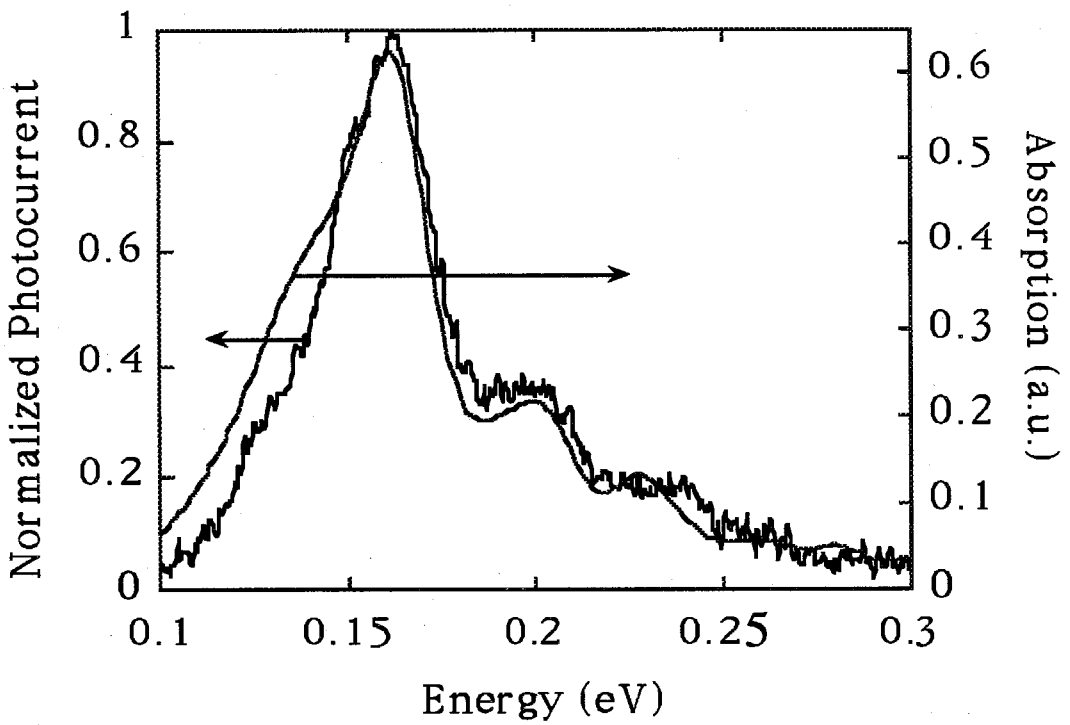

Figure 3-4: Experimental photocurrent spectrum at a bias voltage of -5.0 volts, and the calculated absorption spectrum

Chapter 4

Electron transport in multiquantum well structures

4.1 Introduction

The devices analyzed in this thesis are composed of ultra thin layers of semiconductors. Because of the thickness of layers being smaller than electron de Broglie wavelength in the material, the wave nature of electrons, as predicted by quantum mechanics, is manifested. In chapter 3, studying the optical properties of MQW devices, some of these quantum mechanical effects were discussed, such as formation of energy levels in quantum wells and its effect on the absorption lineshape of intersubband transitions. In this chapter we will see that the current-voltage characteristic of these devices is also affected by electron wave nature, and the simple *effective* point particle description of carriers moving under an external electric field is not valid anymore.

After a brief discussion of the quantum mechanical treatments of carrier transport in MQWs, we will focus on two subjects relevant to the devices which are analyzed: miniband transport and sequential resonant tunneling. We will see how these two phenomena lead to negative differential resistance and electric field domain formation in the device.

4.1.1 Classical transport

The usual method employed to determine the electrical conductivity of bulk semiconductors is to calculate the average value of the current obtained from the probability distribution function, $f(\mathbf{r},\mathbf{p},t)$. $f d\mathbf{r}$ is the probability of finding an electron with crystal momentum $\mathbf{p} = \hbar\mathbf{k}$ in a volume $d\mathbf{r}$ centered at $\mathbf{r}$ at time t.

This distribution function is found by solving the Boltzmann Transport Equation (BTE):

$$\frac{\partial f}{\partial t} + \mathbf{v}.\nabla_r f + q\mathbf{F}.\nabla_p f = \left(\frac{\partial f}{\partial t}\right)_{coll}, \tag{4.1}$$

where $\mathbf{v}$ is the electron velocity and $\mathbf{F}$ the electric field.

The equation is determined by the requirement that in the *steady state* the total rate of change of the distribution function must vanish. This is in turn a sum of the change due to the acceleration by the electric field, and a term due to collisions, which limits this acceleration $((\partial f/\partial t)_{field} + (\partial f/\partial t)_{collisions} = 0)$.

Equation 4.1 is incomplete in several respects. First of all, because of the uncertainty principle, the function $f(\mathbf{r},\mathbf{p},t)$ does not have any precise meaning as a probability function in both $\mathbf{r}$ and $\mathbf{p}$. In fact if wavepackets are formed, then $\Delta r \Delta p \simeq \hbar$, and if the uncertainty in Δp is to be only a small fraction of p (so that we can describe a state with a well defined p), then the spread in the wavepacket in space Δr must be many electron wavelengths long. This is a particularly serious restriction in ultrathin semiconductor structures. Second, the assumption that the scattering takes place locally in space and time is incorrect since the scattering potentials are extended in space and take a finite amount of time to complete. Third, the transition rate is generally calculated by assuming it arises from an incoherent sum of single scattering events. However, if the scatterers are dense (i.e., more than one within a de Broglie wavelength), multiple *coherent* scattering effects are possible. These considerations show that the classical Boltzmann transport equation is not always suited to treat

the problem of electrical conduction in multiquantum wells. In the following we will review various quantum mechanical treatments of transport.

4.1.2 Quantum transport

Density matrix formulation

In quantum mechanics if we wish to find the average of a physical quantity, we need in general not only the probabilities of different states being occupied, but the entire *density matrix*. Now the occupation probabilities of some complete set of states are just the diagonal elements of the density matrix in this representation. Therefore for 4.1 to contain all necessary information, we have to assume that we can find a "natural representation" for our system, and that for this representation the density matrix may be considered diagonal at all times.

Kohn and Luttinger [30], considering a system of electrons in the presence of a homogeneous electric field interacting with randomly distributed impurities, derived a quantum theory of electrical transport based on the entire density matrix. They developed the Liouville equation of motion in ascending powers of the strength of the scattering potential, and recovered the Boltzmann transport equation in the limiting cases of very weak or very dilute scatterers. The treatment of electron transport in multiquantum well structures following Kazarinov and Suris work [26], is based on the density matrix; but for the sake of completeness, we will briefly mention other methods as well.

Wigner functions

The Wigner function is a mathematical transform of the density matrix which approaches the classical distribution function as the system becomes classical. It mimics the averaging of the density matrix operator ρ: $(< A(r,p) >= Tr\{\rho A\}$, where A is the quantity to be measured, which is a function of the *operators* r and p). The Wigner function $P_W(r,p)$ is a function of the *complex numbers* r and p, and it is

defined such that:

$$< A >= \iint \mathcal{A}(r,p) P_W(r,p) dr dp, \tag{4.2}$$

where $\mathcal{A}$ is the Weyl transform of A, and it is a function of r and p which are complex numbers.

The Wigner function is generally nonpositive definite and nonunique, but its time evolution gives a Boltzmann-like transport equation.

Green's functions

This is a more sophisticated approach to quantum transport theory. The nonequilibrium Green's functions are defined as expectation values of single-particle creation and annihilation operators and they describe the state and time evolution of the system. The presence of the energy dependence in the Green's function distinguishes it from the Wigner function. Because the Wigner function measures the state of the device at a particular time and its evolution is described by a first-order differential equation, it can comprehend only external interactions which occur instantaneously in time. The energy dependence of the Green's functions permits a description of the processes which are not local in time, or "non-Markovian" processes, because the energy argument provides a way to include convolution integrals over the past history of the system.

4.2 Electron transport in multiquantum wells

In this section we will see how general methods of quantum transport are applied to study electron motion perpendicular to the layers in a multiquantum well structure. It is shown that at small electric fields, the transport can be described by miniband and hopping conduction, while at large electric fields, the sequential resonant tunneling is manifested. It is useful first to look at the solution of the Schrödinger equation in

the presence of an electric field.

4.2.1 Schrödinger equation with a steady electric field

The Schrödinger equation for an electron in a one-dimensional periodic potential $V(x)$ with a period a and in a static field F has the form:

$$\left(\frac{{p_x}^2}{2m} + V(x) - eFx\right)\psi(x) = E\psi(x), \tag{4.3}$$

where $p_x = -i\hbar(\partial/\partial x)$ is the momentum operator, e is the charge, and m the electron effective mass. In the plane perpendicular to x, the electron behaves as a free electron. Therefore, the corresponding wavefunction has the form $\exp i(p_y y + p_z z)$ with an energy $-(p_y^2 + p_z^2)/2m = -p_\perp^2/2m$. The quantity E in Eq. 4.3 represents the total energy minus the energy corresponding to the transverse motion. The energy spectrum of the system can be obtained on the basis of symmetry considerations. In fact, the translation through n periods of the superlattice transforms Eq. 4.3 into:

$$\left(\frac{p_x^2}{2m} + V(x) - eFx\right)\psi(x - na) = (E - eFan)\psi(x - na). \tag{4.4}$$

Therefore, if the function $\psi(x)$ is an eigenfunction of Eq. 4.3 with an energy E, then the function $\psi(x - na)$ $(\forall n \in N)$ is also an eigenfunction of this equation with an energy $E - eFan$. This implies that the electron energy eigenvalues are split into new levels (Wannier-Stark "ladders") whose mutual distance is eFa. Kane [24], using crystal momentum representation, derived the explicit wavefunction for these energy levels that showed *localization* under the application of an electric field. There have been several objections about this derivation:

Objections about Wannier-Stark ladder and localization

(a) The eigenvalues of the energy are not quantized but are continuous with all values of E allowed.

(b) The Hamiltonian is not periodic on the boundaries of a (finite) crystal because of the scalar potential eFx. It is not clear that one can employ the crystal momentum representation since Bloch functions are periodic on the boundary and a superposition of Bloch functions representing the wavefunction ψ will automatically yield a ψ which is periodic on the boundary.

(c) The crystal-momentum representation of the operator x which enters in the calculation may not be well defined because $xu_{n\mathbf{k}}$ (where $u_{n\mathbf{k}}$ is the Bloch state) can not be represented as a linear combination of Bloch states, i.e., $\int |xu_{n\mathbf{k}}|d\tau$ diverges as the crystal approaches infinite extent in the x direction.

Using a vector potential to preserve the symmetry, Krieger and Iafrate [33] were able to remove these objections. They replaced the scalar potential eFx in the Schrödinger equation with $\mathbf{p} \rightarrow \mathbf{p} - (e/c)\mathbf{A}$, and showed that the calculated optical absorption has the same ladder-like structure that would be obtained if Wannier-Stark quantized energy levels are assumed. Actually the issue is similar to the fact that the states of a Hydrogen atom in a constant field are not discrete, but rather there are narrow *resonances.*

Wannier representation

Keeping in mind the above mentioned resolution of the objections, we return to the original Schrödinger equation 4.3 and seek solution in the form of an expansion in terms of the orthogonal and *localized* Wannier functions (following the treatment by Kazarinov and Suris [26]):

$$\psi(x) = \sum_{n\nu} C_n^{\nu} w_{\nu}(x - na). \tag{4.5}$$

The Wannier wavefunctions are defined by

$$w_{\nu}(x - na) = \frac{1}{\sqrt{N}} \sum_{k} e^{ik(x-na)} u_{\nu k}(x), \tag{4.6}$$

where N is the total number of periods in a crystal, ν the band index and, n the lattice site index. $u_{\nu k}(x)e^{ikx}$ are the Bloch eigenfunctions of the operator $H_o = (p_x^2/2m)+V(x)$. The eigenvalues of this Hamiltonian $E_{\nu k}$ represent the band structure of the problem in absence of an electric field. Here, ν labels the bands and k is the wavevector in a Brillouin "minizone": $-(\pi/a) < k < (\pi/a)$.

In writing the Schrödinger Eq. 4.3 in Wannier representation the following matrix elements are introduced, which are shown pictorially in figure 4-1:

$$I_\nu(n-n') = \frac{1}{N}\sum_k e^{ik(n-n')a}E_{\nu k}, \tag{4.7}$$

$$I_\nu(k) = \frac{1}{N}\sum_{n\neq 0} e^{ikna}I_\nu(n), \tag{4.8}$$

$$X_{\nu\nu'}(n-n') = \int w_\nu(x)xw_{\nu'}(x-an'+an)dx. \tag{4.9}$$

We consider a strong coupling case when the separation between adjacent bands $\Delta_\nu \equiv E_{\nu+1} - E_\nu$ is greater than their widths, which may be denoted by

$$I_\nu \equiv |I_\nu(0) - I_\nu(\pi/a)|. \tag{4.10}$$

In this case, it can be shown that there are two regimes:

Case $eFa << \Delta_\nu$: One finds that the electron energy spectrum is a series of regularly spaced levels (Wannier-Stark ladder), and the corresponding wavefunctions are localized in each cell. If the energy eFa is lower than the width of the allowed band I_ν, the electron is essentially localized within the space I_ν/eFa.

Case $eFa \simeq \Delta_\nu$: Now the ground state of a site is aligned with the excited state of the adjacent site. It can be shown that in this situation, in the absence of collisions and intra-site relaxation, the peak of the electron probability density oscillates back and forth between the two sites with a frequency equal to

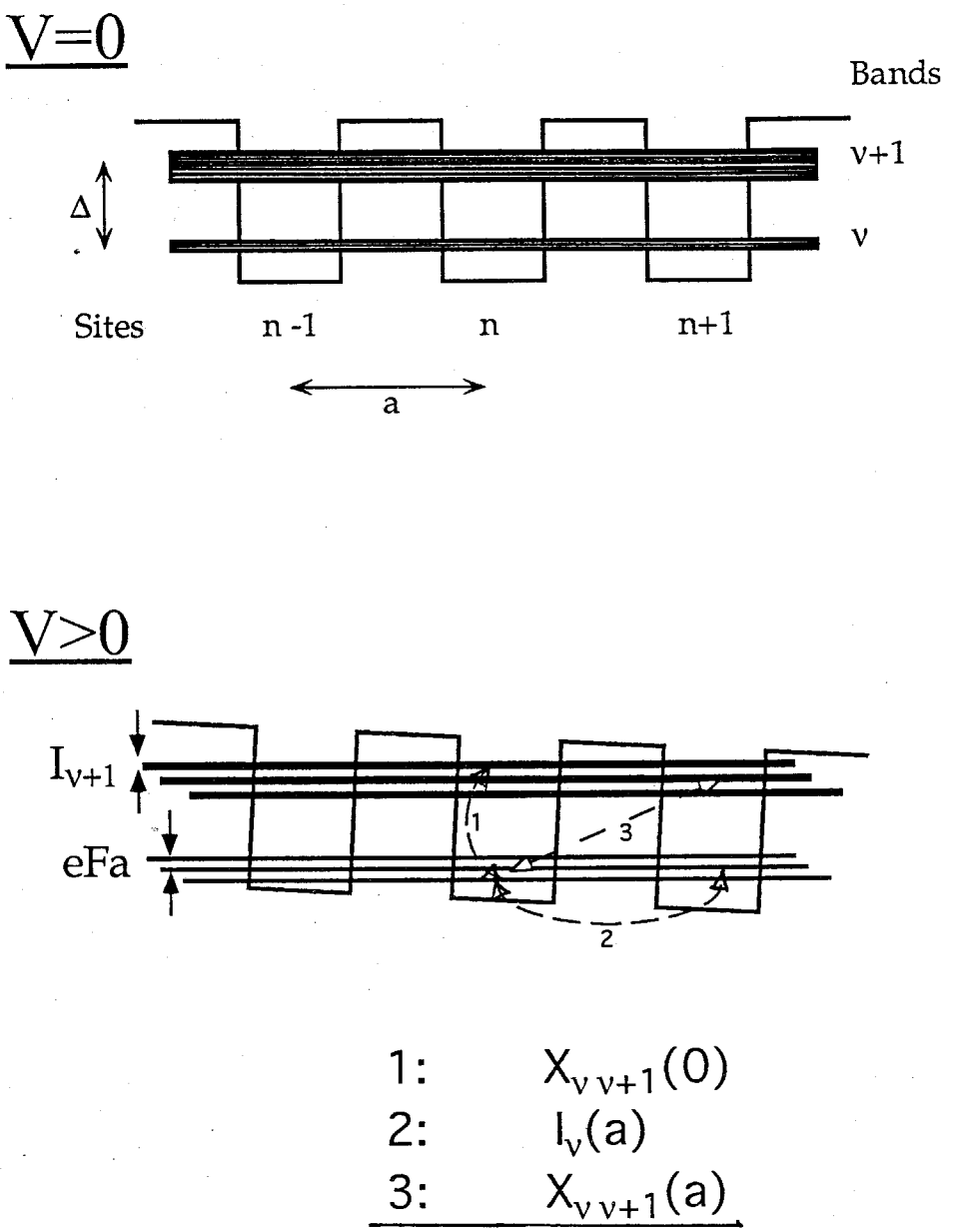

Figure 4-1: Multiquantum well energy levels under an electric field, showing the Wannier-Stark ladder and various matrix elements describing the interaction between levels.

$\Omega = eFX_{12}$. This is very similar to Rabi oscillations observed in the coherent interaction of light with two-level systems (such as in the case of paramagnetic spin resonance).

In both of these cases, there is no net current flowing. It is the presence of collisions and scattering, in combination with the above mentioned evolutions, which produce a current. Carrier transport in the presence of scattering is the subject of study in the next section.

4.2.2 General treatment of carrier transport in superlattices

Recently Laikhtman and Miller [36,37] treated the problem of current transport perpendicular to the layers in a superlattice using the Keldysh technique to drive a kinetic equation for the electron density matrix. This technique, based on the Dyson equation for the Green's functions, can treat the problem of conductivity of multi-quantum wells, for an *arbitrary* relation between the width of the subbands (I_ν given by equation 4.10), the electric potential drop per period (eFa), and the energy uncertainty due to scattering (Γ). All these energies, however, are considered to be much smaller than the width of the electron energy distribution in each layer of the superlattice. This assumption, which arises because of the in-plane electron motion, justifies a perturbative calculation of the transport properties. Laikhtman and Miller found the following expression for the transition probability (w) between two energy levels in adjacent wells:

$$w \propto \frac{\Lambda^2}{\hbar} \frac{\Gamma}{\Gamma^2 + \Delta^2}, \tag{4.11}$$

where Δ is the energy separation between levels, Γ the level width due to elastic scattering, and Λ the overlap integral between the wavefunctions of the two levels (It can be shown that 4Λ is the intrinsic width of the subband (I_ν), see section 4.2.3).

This transition probability gives the following expression for the electric current from the νth level in the nth well to the ν'th level in the $(n+1)$th well:

$$j_{\nu\nu'} = \frac{e}{\hbar}\int \frac{2d\mathbf{p}}{(2\pi\hbar)^2}\frac{2\Gamma\Lambda_{\nu\nu'}^2}{\Gamma^2+\Delta_{n,\nu\nu'}^2}\left[\rho(E_{\mathbf{p}})-\rho'(E_{\mathbf{p}}+\Delta_{n,\nu\nu'})\right], \tag{4.12}$$

where ρ is the density of states. In the case of tunneling between ground states ($\Delta_{n,11} = eFa$), one recovers Ohm's law for $eFa << \Gamma$, and $j \propto 1/F$ in the opposite situation.

The above mentioned treatment is quite general and it can reproduce the I-V characteristics of multiquantum well structures. It was used to study the current-voltage instabilities [36], and electric field domain formation [37] in superlattices. It is still more intuitive to derive the electrical properties of MQWs directly in some limiting cases. This gives more insight about different mechanisms which affect the electron traveling perpendicular to the layers in a MQW structure [62]. In the following, depending on the parameters Λ, Γ, and eFa, we will distinguish two regimes:

- If $eFa << \Gamma << \Lambda$ (miniband regime) the Stark levels are not resolved and the electron transport can be described by classical Boltzmann transport equation.
- If $\Gamma >> \Lambda$, $\forall eFa$ (hopping regime) the electrons are scattered after each tunneling across a barrier and no minibands exists. The transport is by hopping between adjacent wells of the superlattice. In this regime whenever the energy levels of adjacent wells are aligned, there is *resonant* tunneling between them.

We will first describe with more details these two limiting cases, and we will see that both of these give rise to negative differential resistance and instabilities in the I-V characteristics.

4.2.3 Miniband transport

In this case the superlattice is considered as a perfect crystal in which both the electric field and the various scattering act as weak perturbations. The simplest band model

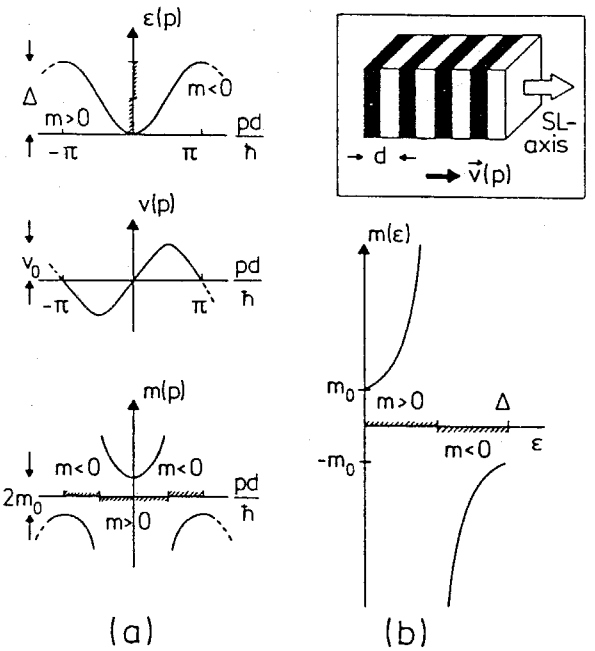

Figure 4-2: Energy, velocity, and effective mass of an electron in a superlattice miniband as a function of crystal momentum [22].

is the tight-binding one which leads to an energy versus wavevector relationship as [50]:

$$E(\mathrm{k}) = \epsilon(k_y, k_z) + 2\Lambda\left(1 - \cos(k_x a)\right), \tag{4.13}$$

in which $\epsilon(k_y, k_z)$ is the parallel kinetic energy, x the growth direction, 4Λ the miniband width and a the superlattice period. The average group velocity along the superlattice axis (drift velocity) is obtained from 4.13 (see figure 4-2):

$$v_x = \left(\frac{1}{\hbar}\frac{dE}{dk_x}\right) = \frac{2\Lambda a}{\hbar}\sin k_x a \tag{4.14}$$

From the acceleration theorem $\hbar(dk_x/dt) = eF$, we see that the electron wavevector grows proportionally to time, $k \sim eFt/\hbar$. Such a free acceleration can last no longer than the relaxation time $\hbar/\Gamma$. If the scattering is very weak equation 4.14

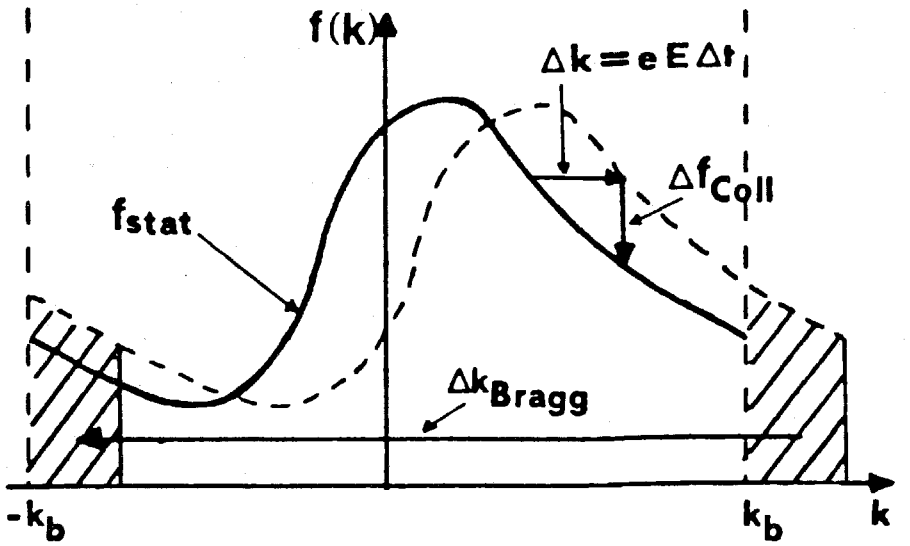

Figure 4-3: Change of the distribution function due to acceleration by the field F, to ordinary scattering processes, and to Bragg scattering [3].

shows that the constant electric field induces an oscillatory electronic motion in k-space. The time period for these so called "Bloch oscillations" is given by h/eFa. *The Wannier-Stark states described in section* 4.2.1 *are, in fact, the stationary counterpart of the time-dependent description above.*

Assuming a relaxation-time approximation with collision time $\hbar/\Gamma$, the Boltzmann equation gives:

$$< v_x >= \frac{2\Lambda a}{\hbar} \frac{I_1(2\Lambda/k_BT)}{I_0(2\Lambda/k_BT)} \frac{eFa/\Gamma}{1+(eFa/\Gamma)^2}, \tag{4.15}$$

in which I_n is the modified Bessel function. The factor I_1/I_0 accounts for reduction of the drift velocity at elevated temperatures describing thermal saturation of the miniband transport in a superlattice. Equation 4.15 shows that there is a critical field ($\propto (\Gamma/a)$), above which there is negative differential velocity. This result, first pointed out by Esaki and Tsu [12], is due to Bragg reflections from the zone-boundary

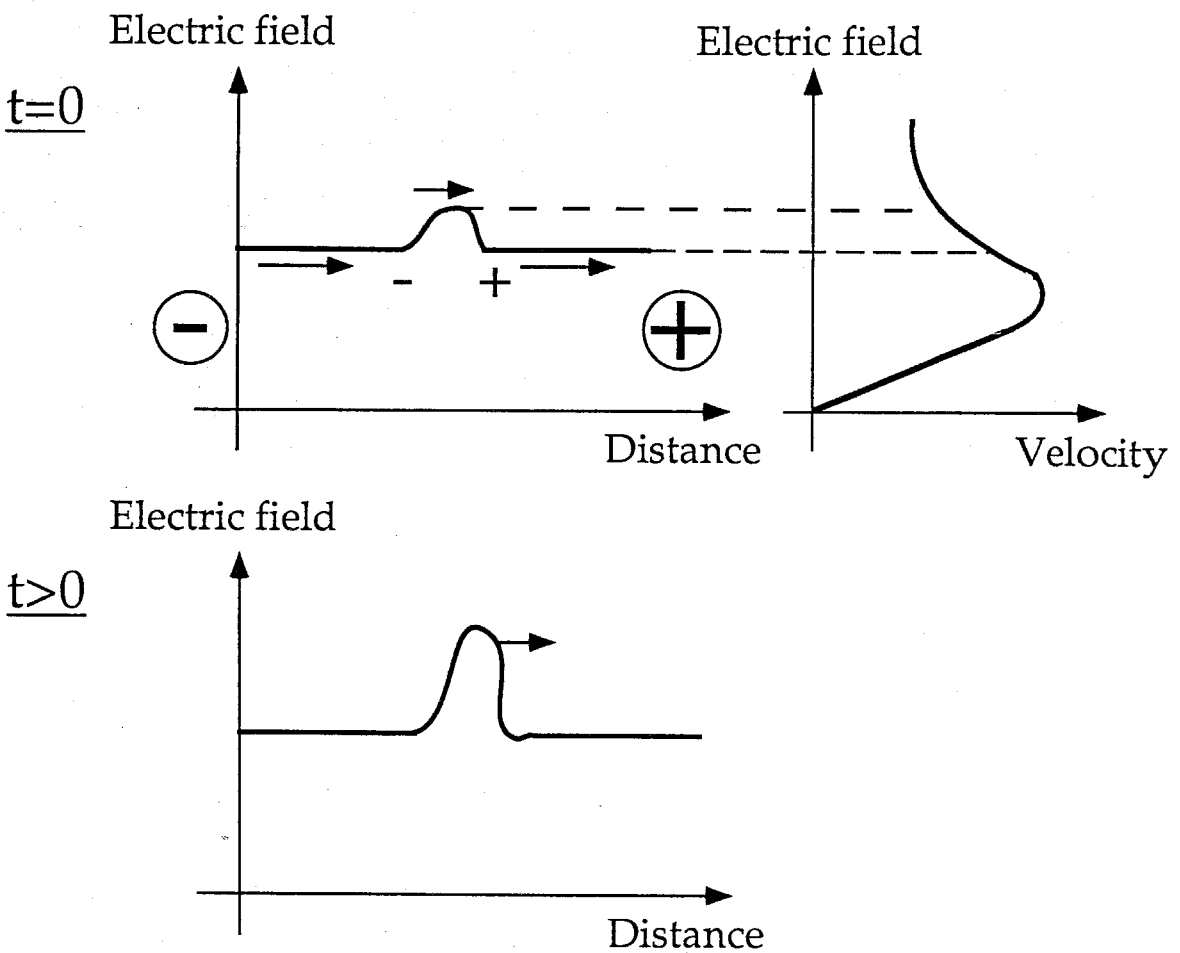

Figure 4-4: Negative differential velocity and domain formation

GaAs. In the next paragraphs the formation of electric field domains in single crystal *GaAs* is briefly reviewed, and some important observations of voltage instabilities in superlattices are mentioned.

4.3.1 Electric field domains in bulk semiconductors

The formation of electric field domains (EFD) was first observed in bulk *GaAs* and *InP* and is mostly known as the cause of Gunn oscillations [16]. In 1963, when J.B. Gunn was studying the current-voltage characteristics of *GaAs* and *InP* devices, he

discovered that when the applied electric field was greater than some critical value of several thousand volts per centimeter, spontaneous current oscillation appeared in the circuit. Using probe measurements of the potential distribution across the sample, he established that a propagating high field domain forms in the sample. It nucleates near the cathode, propagates toward the anode with velocity of the order of $10^5 m/s$, and disappears near the anode. Then this process repeats itself. The domain formation leads to a current drop, the domain annihilation results in an increase in the current, and periodic current oscillations exist in the circuit. Later, Kroemer pointed out [34] that all the observed properties of the microwave oscillation were consistent with a theory of negative differential resistance independently proposed by Ridley and Watkins [55] and by Hilsum [20]. The mechanism responsible for the negative differential resistance is a field-induced transfer of conduction-band electrons from a low-energy, high-mobility valley to higher energy, low-mobility satellite valleys. Using the Poisson equation and the equation of current continuity, it can be shown [72,75] that a semiconductor exhibiting bulk negative differential resistivity is inherently unstable, because a random fluctuation of carrier density at any point in the semiconductor produces a momentary space charge that grows exponentially in time (see figure 4-4). Eventually this leads to the formation of high and low field domains in the sample. The continuity of the current requires in most cases that the high field domain moves from the cathode to the anode.

4.3.2 Electric field domains in multiquantum wells

Miniband conduction regime and the associated negative differential velocity

We saw that in the miniband conduction regime (i.e. when the applied bias per superlattice period is smaller than the width of the miniband), electrons accelerated perpendicular to the layers may exhibit negative differential velocity due to the negative effective mass and Bragg reflections that they would experience. And this would

give rise to negative differential conductivity. Recently, Sibille et al. [51] and Beltram et al. [5] have observed Esaki-Tsu negative differential velocity in superlattices. Le Person et al. have observed Gunn oscillations in the growth direction of a nonintentionally doped $GaAs/AlAs$ superlattice [52]. And finally, the Bloch oscillations were directly observed by detecting the submillimeter-wave emission from coherent charge carrier oscillations in a superlattice [29].

Hopping conduction and resonant tunneling regime and the associated negative differential resistance

Another negative differential conductance mechanism in superlattice structures was observed by Esaki and Chang [13] in 1974, when the miniband conduction was broken. They studied the transport properties of a $GaAs$(4.5nm)/$AlAs$(4.0nm) superlattice. Because of the thin barriers, there is a strong coupling between wells which produces a large ground-state bandwidth (5meV) and thus the electron transport is by miniband conduction. By studying the I-V characteristics, they observed an oscillatory negative conductance due to the formation of an expanding high field domain produced by the electric field induced breaking of the miniband conduction. The voltage drop across this domain aligns the ground state of one well with the first excited state of the neighboring well allowing resonant tunneling to occur. A similar phenomenon was observed by Choi et al. in the case of weakly coupled quantum wells [10]. In this case the superlattice consisted of 49 periods of $GaAs$(7.6nm)/$Al_{0.27}Ga_{0.73}As$(8.8nm) multiquantum wells. The ground state bandwidth being 0.4meV, the quantum well states are localized (by well width fluctuations and also by applied voltage). Therefore electron transport is dominated by sequential resonant tunneling (SRT). In spite of important differences in transport mechanism (between miniband conduction and SRT), Choi et el. observed similar negative conductance oscillations in the I-V characteristics. SRT was first studied theoretically by Kazarinov and Suris in 1971 [26], who predicted the existence of peaks in the I-V characteristics of weakly coupled

multiquantum wells (tight-binding superlattices), which correspond to resonant tunneling between the ground and excited states of adjacent wells. Later, Capasso et al. observed these peaks in a $AlInAs/GaInAs$ superlattice [4]. Recently, in addition to transport experiments which showed high field domain formation, there have been optical studies of these domains in superlattices. Grahn, Schneider et al. used Stark shift in the photoluminescence spectra to identify different electric field domains in a $GaAs/AlAs$ superlattice [15].

4.4 Conclusion

In this chapter the main features of the carrier transport in multiquantum well structures were reviewed. Depending on the applied bias, coupling between wells, and scattering, different regimes of miniband conduction and hopping transport were identified. In both cases current-voltage instabilities are observed. Their physical origin is due to Bragg reflections over the miniband's zone boundary, and resonant tunneling between adjacent wells, respectively.

Chapter 5

Negative differential resistance and domain formation in multi-stack quantum well infrared photodetectors

In chapter 4 we saw that electron transport perpendicular to the layers in multiquantum well structures, has different regimes of miniband conduction, hopping transport, and sequential resonant tunneling, depending on the applied bias, width of the minibands, and broadening due to the various scattering. We also saw that these transport mechanisms can give rise to negative differential resistance, which in some cases leads to the formation of electric field domains in the multiquantum well region. In this chapter we will see how the switching behavior of the photocurrent response of multi-stack quantum well detectors, under different biases, can be explained by the formation of electric field domains.

5.1 Introduction

Quantum well infrared photodetectors (QWIPs) are based on intersubband transitions[74, 43,27]. As it was discussed in chapter 3, when a thin $GaAs$ layer is surrounded by wider band gap material such as $AlGaAs$, electron motion perpendicular to the layers is quantized. This creates a series of subbands in the conduction and valence band. If

the quantum well is, for example, n-doped, the lowest subband in the conduction band is populated with electrons. Now under an incident infrared radiation these electrons can be excited to a higher subband. This is called a bound-to-bound transition when the second subband is below the top of the well, and a bound-to-continuum transition in the case where the excited state is above the barrier. An electric field applied perpendicular to the layers, collects the photoexcited carriers, and a photocurrent can thus be measured.

These detectors usually have a narrow spectral range of detection ranging in width around $10 - 20\%$ of the peak wavelength [43]. In some applications this could be considered an advantage; in many other situations one would like to achieve as broad a range of detection as possible. A second issue which can be seen as limiting in many applications is the lack of flexibility, as for the peak wavelength and the whole spectral range, once the device has been designed and grown [41,57].

Recently, Gravé et al. [63] proposed and demonstrated a new type of QWIP, consisting of different stacks of quantum wells arranged in series. All the wells in a given stack are identical, but each stack is designed for absorption and detection at a different wavelength, featuring distinct well widths and barrier heights. This detector can operate as a multi-color voltage controlled IR detector or as a broad band detector depending on the bias [63,64]. In the following sections we will discuss design and characterization of this detector, and we will see how the analysis of the photocurrent spectrum and the dark current enables one to study different transport mechanisms of optically or thermally excited electrons in these structures. We will also discuss the evidence for sequential resonant tunneling induced electric field domain formation in the multiquantum well region.

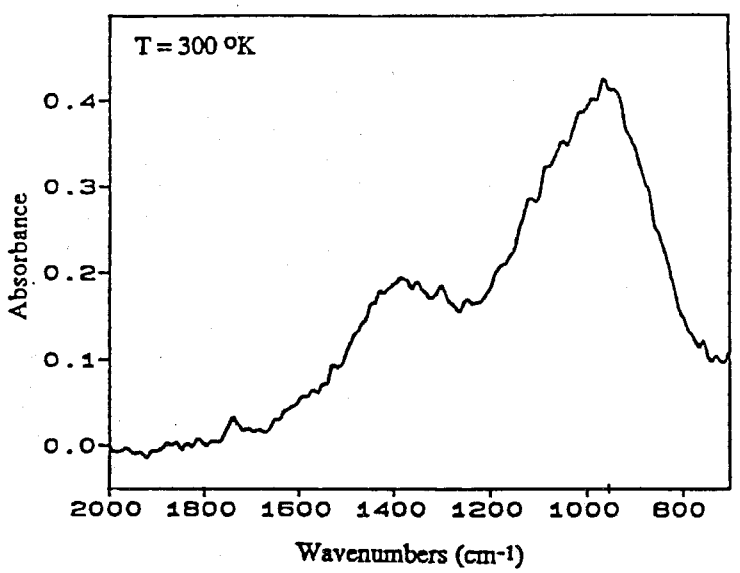

Figure 5-1: Absorption spectrum at room temperature. The measurement was performed with a Fourier transform spectrometer using a 45° multipass geometry; the spectrum is normalized to reflect the contribution of the intersubband absorption alone. An absorption coefficient α_{45}=600 cm^{-1} for the peak at 1364 cm^{-1} was derived. The inset shows the device structure.

5.2 Sample structure and characterization of the multi-stack infrared detector

The structure was grown by molecular beam epitaxy on a semi-insulating GaAs substrate. The multiquantum well region, clad by two n-doped contact layers, consisted of three stacks of 25 quantum wells each; the first 25 wells (called stack (a)) were 3.9 nm wide and were separated by $Al_{0.38}Ga_{0.62}As$ barriers; the second stack (b) consisted of 4.4 nm wide wells with $Al_{0.30}Ga_{0.70}As$ barriers; the last stack (c) had 5.0 nm wide wells and $Al_{0.24}Ga_{0.76}As$ barriers. All the barriers were 44 nm wide; the wells and the contacts were uniformly doped with Si to $n = 4 \times 10^{18} cm^{-3}$ (a schematic of the device is drawn in the inset of figure 5-1).

5.2.1 Absorption spectrum

The absorption spectrum at zero field and room temperature is shown in Figure 5-1. The measurement was taken with a Fourier transform infrared spectrometer in the usual 45° multipass geometry [38]; the absorption of the light polarized in compliance with the selection rules was normalized by the absorption of light polarized in the perpendicular direction, to allow for only the intersubband contribution. The absorption peak at 1364 cm^{-1} is due to the 3.9nm wells while the stronger absorption at 964 cm^{-1} is the composite contribution of the two other stacks of quantum wells, which, individually, have absorption peaking at 1080 and 920 cm^{-1}. These results agree with our design values; our calculations, which included band nonparabolicity [80] and a band offset value of 0.60, anticipated absorption peaks at room temperature at 1335, 1052, and 880 cm^{-1}, respectively. We see that in each of the three different types of wells, light is absorbed by electrons excited from the first subband to a second subband which is located close to the top of the well.The existence of the two absorption peaks that merge into a wide and strong peak was also experimentally verified by analyzing the absorption of a few additional MBE grown control wafers, which were designed to include, each time, only two of the stacks described above.

5.2.2 Photocurrent spectrum

Devices were processed out of the grown wafer and prepared as etched mesas, 200μm in diameter. Figure 5-2 displays the photocurrent spectroscopy of a device at a temperature of 10K, for positive values of applied voltage. It is seen that, for low applied fields ($\leq 5V$), the stack (a) of 3.9nm wells, closer to the substrate, provides most of the photocurrent at the appropriate excitation energies around the peak of 1450 cm^{-1}. When the bias is increased to 6V, the contribution of stack (a) increases while the contribution of the other two stacks *disappears*. Increasing the bias even further (to 7V) reduces the photocurrent peak at 1450 cm^{-1}, but the other two stacks start to contribute again. When the bias reaches a threshold of 8V, a sharp

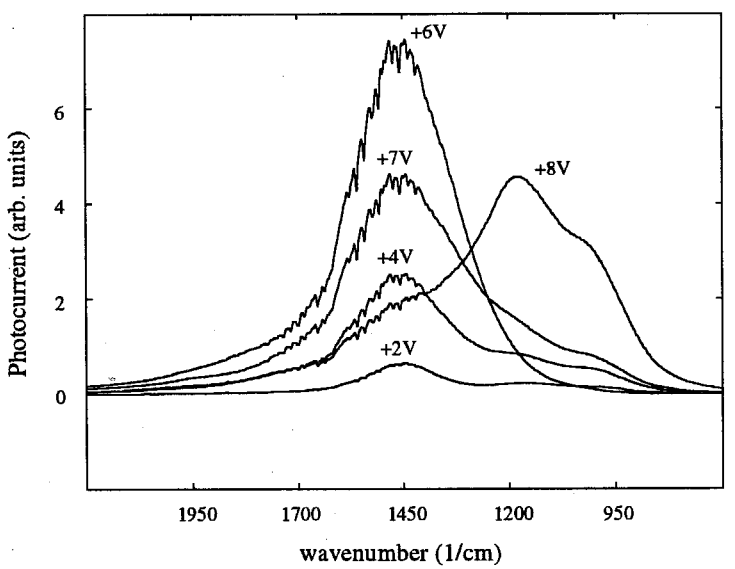

Figure 5-2: Spectral photoresponse for a few values of applied positive voltage. Note the switching in peaks at an applied voltage around $8.0V$. The responsivity, at the peak of $1140cm^{-1}$ and the applied voltage of 8.0V, is 0.75 A/W. The units are the same for both Figure 5-3 and Figure 5-2.

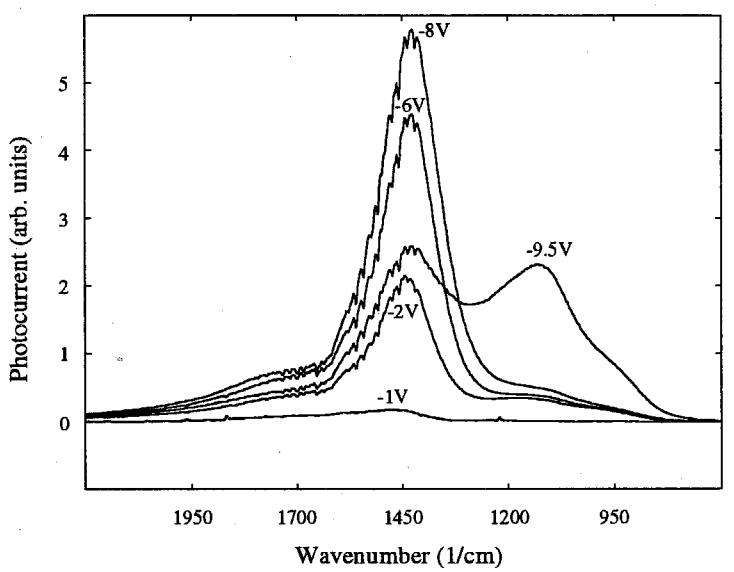

Figure 5-3: Spectral photoresponse for a few values of applied negative voltage for the three-stack quantum well infrared photodetector. Note the broadening in the spectral response below $-9.0V$.

transition takes place and the responsivity peak *switches* to 1190 cm^{-1}. It is apparent that stack (b) and (c) are now responsible for most of the photocurrent, while the contribution from the stack (a) has sensibly decreased. Note that the small shifts of the photocurrent peaks with regard to the absorption peaks are due to the different experimental temperatures [42] and to the applied electric field [17] (see also [56]).

If we apply a negative bias to the detector [see figure 5-3], again, at low voltages, the photocurrent is due mostly to electrons excited in the stack (a). The responsivity increases with the applied voltage, but its magnitude is always less than that corresponding to the same forward bias; in addition, one observes that the photocurrent peak around 1450 cm^{-1} is $\approx$ 50% broader in the forward bias mode. When the bias is increased to more negative values (-9V), the responsivity extends to lower energies, showing increasing contributions from stack (b); stack (a) still contributes equally, in contrast to the sharp reduction in response experienced in the opposite polarity of the applied electric field.

These features in the photocurrent, which are observed at a temperature of 10K, persist at higher temperatures. In the reverse bias direction, one observes the same general behavior also at 77K. In the forward polarity, the switching of the photoresponse from the higher energy peak to the lower one is observed up to a temperature of 60K; the critical voltage at which the switching occurs increases slightly with temperature.

5.2.3 Current-voltage characteristics

The I-V curves of the device at different temperatures are shown in Figure 5-4. One can note a strong asymmetry between the two polarities. A fine structure in the plateau of the I-V curves, corresponding to regions of negative differential resistance, was observed. For example the T=10K curve has oscillations in the voltage range of -10.0 to -7.0 volts and +4.0 to +7.0 volts. In each of these intervals 24$\pm$2 oscillations with a period of 0.128$\pm$0.008 volts were measured. Figure 5-5 shows an expansion

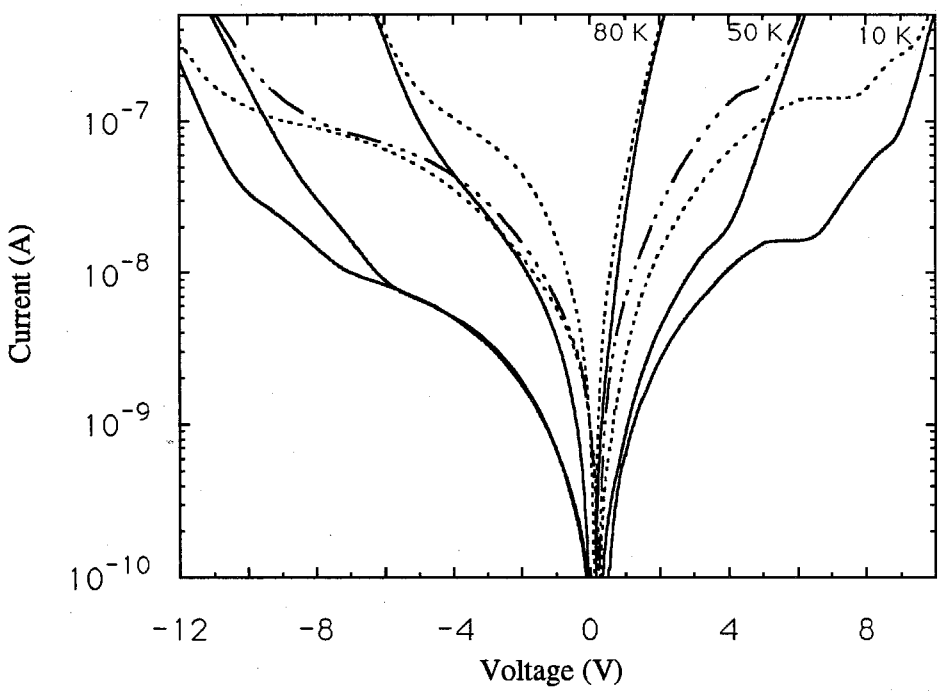

Figure 5-4: I-V characteristic at different temperatures. The solid curves are without illumination and the dashed ones are with illumination of a black body source. Note the important contribution of photo-assisted transport to the total current, specially at low biases.

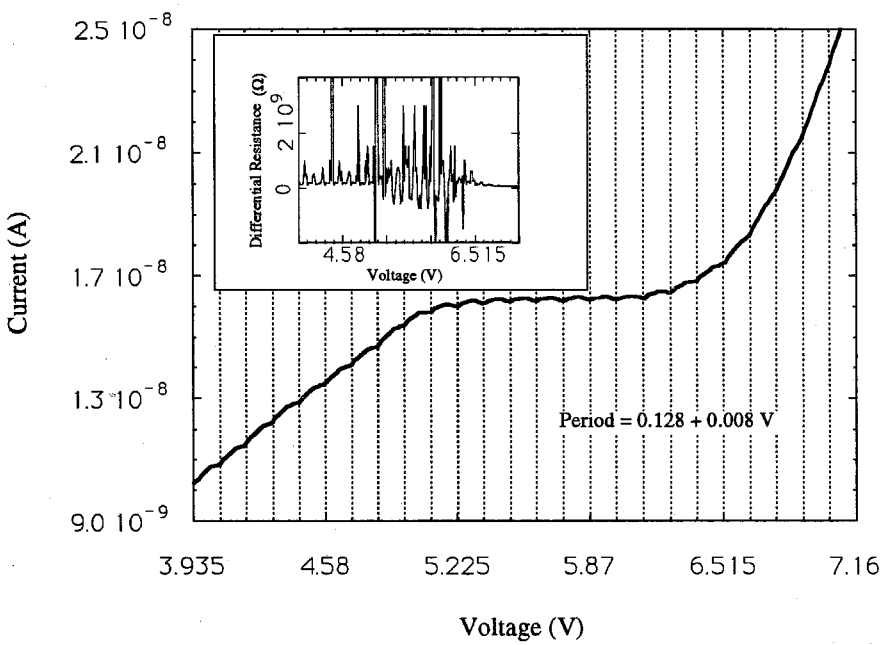

Figure 5-5: An expansion of the [+4,+7] range in the 10K I-V curve (without illumination). One can see 24 oscillations with a period of 0.128±0.008 volts. The inset shows oscillations in the differential resistance of the device.

of the forward bias plateau region. One can see in the inset, the oscillations of the differential resistance of the device. This measurement gives a most important clue to the possible origin of photocurrent peaks disappearing and switching, since these negative differential resistance oscillations are the signature of the formation and expansion of a high field domain along the sample multiquantum well region [13,10,26,4,15,36].

The data of the photocurrent spectral measurement were taken with a Fourier transform spectrometer, complemented by a setup including a calibrated black-body source and a set of cooled filters at different wavelengths. The noise equivalent voltage was measured directly with a spectrum analyzer in the cold, shielded window configuration. One should also note the very low values of dark current, which, combined with a responsivity ranging up to 0.75 A/W, ultimately yield high D^* for this detector (D^*=4×10^{11} $cmHz^{1/2}W^{-1}$ at 40K and 1140 cm^{-1}).

5.3 Interpretation of experimental results

We saw in the previous chapter that when a series of quantum wells are under large applied bias, a uniform distribution of electric field is not *stable* because all of the quantum wells will be out of resonance, i.e. none of the energy levels of pairs of adjacent wells will be aligned. Instead, the system will settle into a configuration in which the electric field profile includes high and low field regions (see figure 5-6). In the high field region we have ground level to excited level sequential resonant tunneling, and in the low electric field region ground level to ground level tunneling. Transport within each domain is thus resonant, while at the boundary between the two regions it is generally non-resonant. This boundary then acts as a bottleneck that limits the current. Charge accumulation or depletion at this boundary takes place because of the change in the slope of electric fields, as required by Poisson's equation. An increase in the bias will cause more quantum wells to enter the high field domain

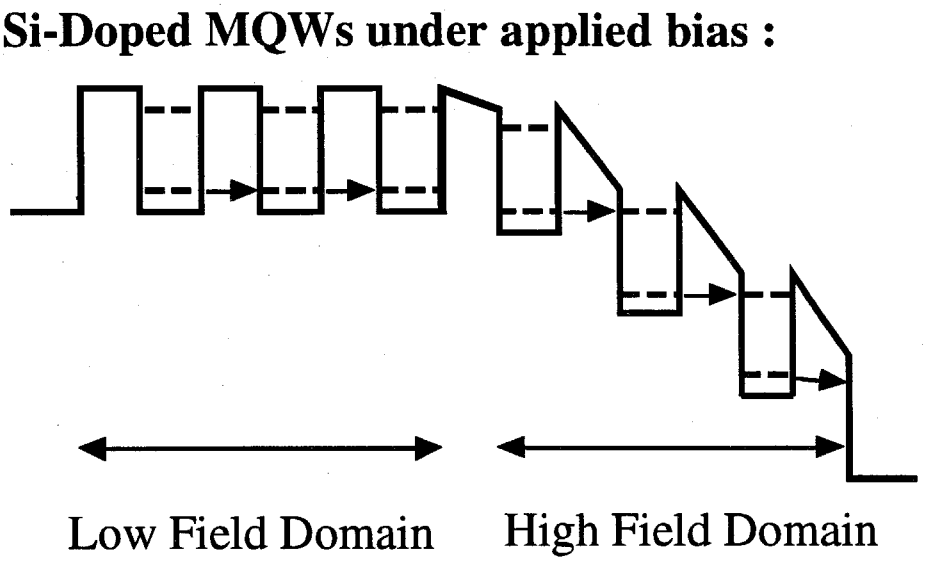

Figure 5-6: Formation of high and low field domains in the case of a weakly coupled Si-doped $GaAs/AlGaAs$ multiquantum well structure

region, and this is reflected by the oscillatory behavior in the I-V curve.

Under illumination, the light is absorbed in all the quantum wells but only photoexcited carriers which are in a region with a high electric field can be swept out of the quantum well and contribute to the photocurrent. Those in the low field region have a high probability of being recaptured by their own well, contributing negligibly to the photocurrent. The observed oscillations in the I-V curve are in the same voltage range where photocurrent peak disappearance and switching occurs. This is an indication that electric field domain formation can be responsible for the observed behavior in the photocurrent spectrum. On the other hand, the low bias behavior of this device did *not* show any negative differential resistance, and different contribution of the three stacks to the photocurrent can be explained using Liu's equivalent circuit analysis [45].

The presence of plateaux in the I-V characteristic is consistent with the current being limited by the boundary between high and low field domains (see e.g.

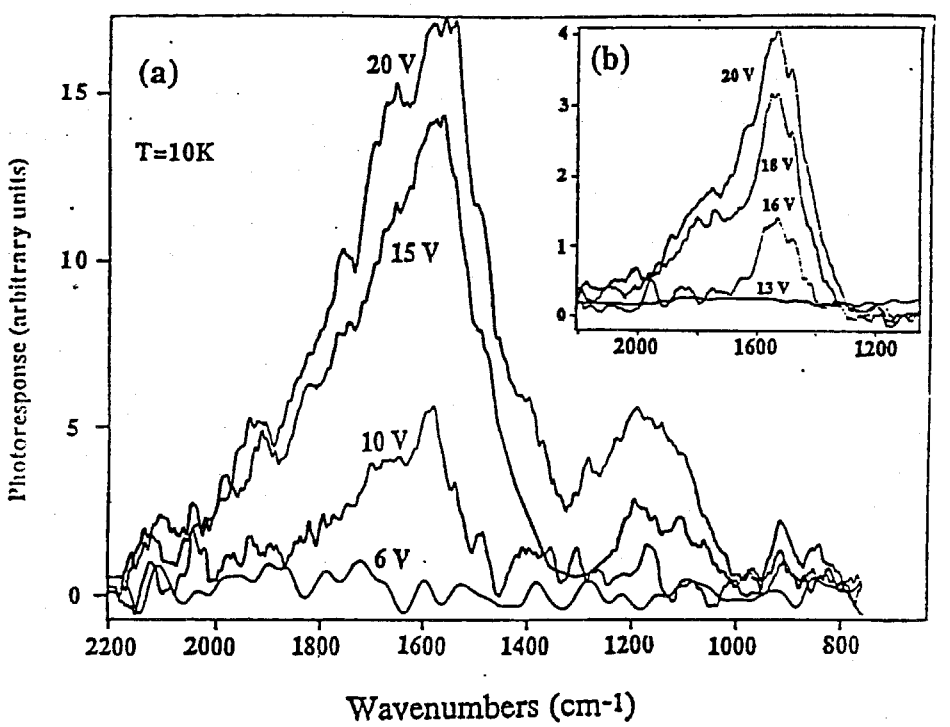

Figure 5-7: Spectral photoresponse for the two-stack MQW device with $44nm$ barriers in both stacks. At low bias there is a peak at $\approx 1600cm^{-1}$ and as we increase the applied bias another peak at *longer* wavelengths $\approx 1200cm^{-1}$ appears. (Inset) Spectral photoresponse of another two-stack MQW device with similar well characteristics but the barriers in the long wavelength stack are shortened to $20nm$. At low bias there is a peak at $\approx 1550cm^{-1}$ and as we increase the applied bias another peak at *shorter* wavelength $\approx 1800cm^{-1}$ appears.

refs.[10,15]). The period of oscillation (0.128 ± 0.008 volts) is close to the separation between ground state and the excited state in stack (c) (123 meV). However, for these bound-to-continuum detectors where the excited state is near the quantum well edge (typically 10 meV above the barrier), it is possible that sequential resonant tunneling does not occur to the states which are maximally localized in the well region (corresponding to the absorption peak).

5.4 Design of multi-stack infrared photodetectors

Even though there are a lot of processes and parameters which can influence the transport in the superlattice, such as impurity or phonon-assisted tunneling, resonant tunneling through different states in the continuum, relaxation times and space charge effects; it is still possible to design samples with the desired responsivity peaks for applications like tunable multi-color infrared detectors [64]. This is done by considering the charge accumulation effects at the boundaries between different stacks, and at the boundary between high and low field domain.

Figure 5-7 shows the photocurrent spectroscopy at different applied biases for a two-stack MQW IR-detector with a design similar to that of our original three-stack device (stack (a):4.0 nm $GaAs$ wells separated by 44 nm $Al_{0.36}Ga_{0.64}As$ barriers. Stack (b):5.2 nm $GaAs$ wells separated by 44 nm $Al_{0.24}Ga_{0.76}As$ barriers). At low bias there is a peak at short wavelengths $\approx 1600cm^{-1}$ and as we increase the applied bias another peak at longer wavelengths $\approx 1200cm^{-1}$ appears.

Figure 5-7(inset) displays the photocurrent of a second two-stack MQW detector where the barriers in the stack (b) (having absorption peak at longer wavelength) were shortened to 20 nm (stack (a):4.0 nm $GaAs$ wells separated by 44 nm $Al_{0.38}Ga_{0.62}As$ barriers. Stack (b):4.7 nm $GaAs$ wells separated by 20 nm $Al_{0.30}Ga_{0.70}As$ barriers). By this means we can achieve the requirement that the electric field for the ground state to excited state SRT be increased in stack (b) and become larger than the corresponding value of the electric field in stack (a). As a result we see that this time the peak at longer wavelength ($\approx 1550cm^{-1}$) appears first, and then, by increasing the bias further, the peak at shorter wavelength ($\approx 1800cm^{-1}$) appears.

5.5 Conclusion

Evidence was presented for sequential resonant tunneling induced negative differential resistance in very weakly coupled quantum wells (separated by 44nm barriers). This is an indication of electric field domain formation in the device. As electrons which are

photoexcited in each quantum well, can sweep out and contribute to the photocurrent only when there is a large enough electric field assisting them; the photocurrent is dominated by the wells in the high field region. Now if the quantum well widths and barrier heights are not the same at different places of the superlattice (i.e. in the case of multi-stack device); the photocurrent spectrum can be tuned by changing the applied bias; which changes the electric field distribution.

Chapter 6

Small bias behavior of the photocurrent spectrum in quantum well infrared photodetectors

In this chapter an abnormal low bias behavior of the photocurrent spectrum in quantum well infrared photodetectors (QWIPs) is reported [70], and its possible origin due to the doping segregation during the MBE growth is discussed.

6.1 Sample structure and its characterizations

The sample analyzed for this study was grown by molecular beam epitaxy on a semi-insulating GaAs substrate. It consisted of 25 periods of $5.4nm$ $GaAs$ wells separated by $42.5nm$ $Al_{0.30}Ga_{0.60}As$ barriers. The multiquantum well region was clad by two $0.5\mu m$ n-doped contact layers. The wells and the contacts were uniformly doped with Si to a concentration of $n = 5 \times 10^{18} cm^{-3}$.

The quantum well width and the barrier height in this device are such that there are two stationary states for electrons with an energy smaller than the barrier height (i.e. this is a bound-to-bound detector). The oscillator strength of the transition between these two states is very large ($f_{12} \approx 0.9$). This is because both of these states are localized in the well region. The oscillator strength which is proportional to the dipole matrix element is basically the overlap integral of these two state's wavefunctions with the position operator:

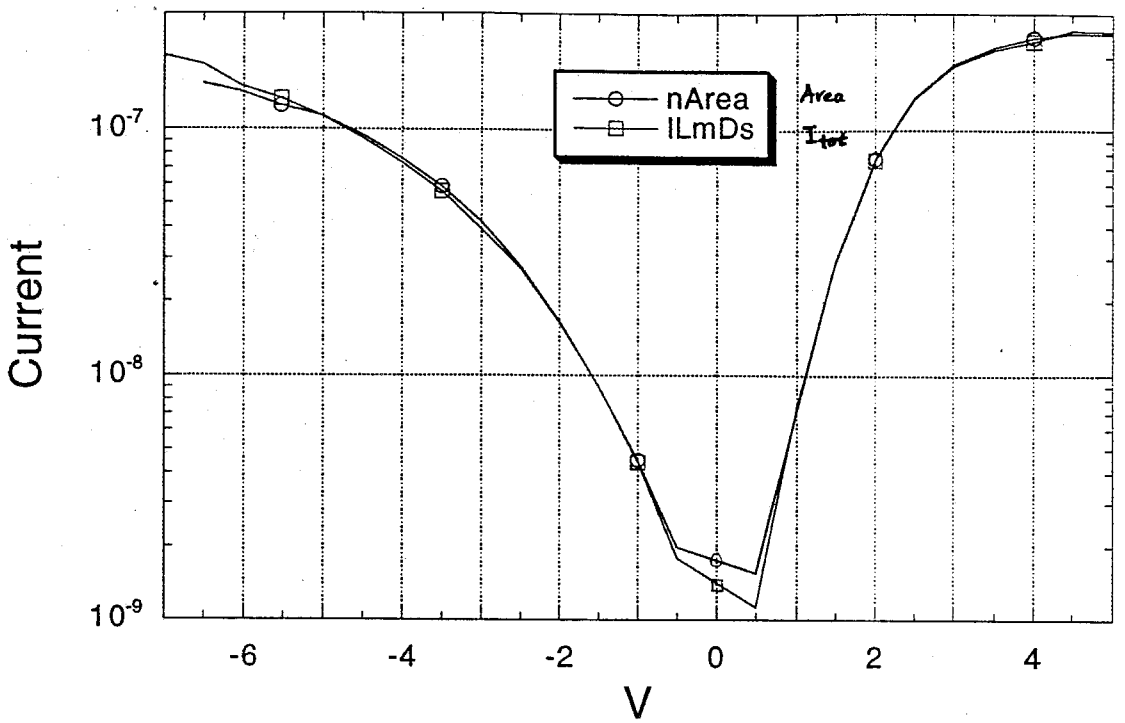

Figure 6-1: Integrated photocurrent of the device as a function of applied bias, at a temperature of $10K$.

$$f_{12} = \frac{2m^*}{E_{12}}\langle 1|\mathbf{r}|2\rangle. \tag{6.1}$$

This discrete and large oscillator strength gives the absorption spectrum a Lorentzian lineshape. The width of the Lorentzian is due to various scattering mechanisms (interface, impurity and alloy disorder scattering), non-parabolicity and many-body effects. The optical transition to the states above the barrier is possible, but their contribution is very small. This could be seen from the oscillator strength sum rule (see chapter 3):

$$\sum_{j\neq 1} f_{1j} = 1. \tag{6.2}$$

Figure 6-1 shows the integrated photocurrent of these detectors measured at a

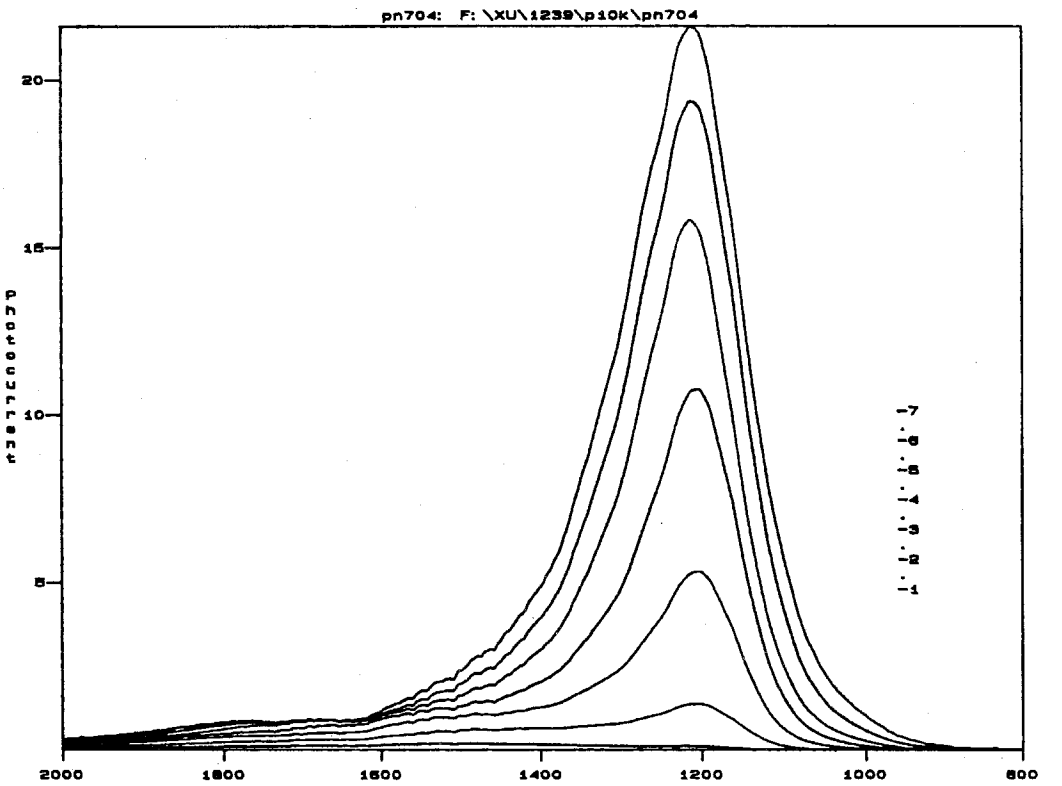

Figure 6-2: Photocurrent spectrum for large values of applied negative bias (defined with respect to the bottom contact layer).

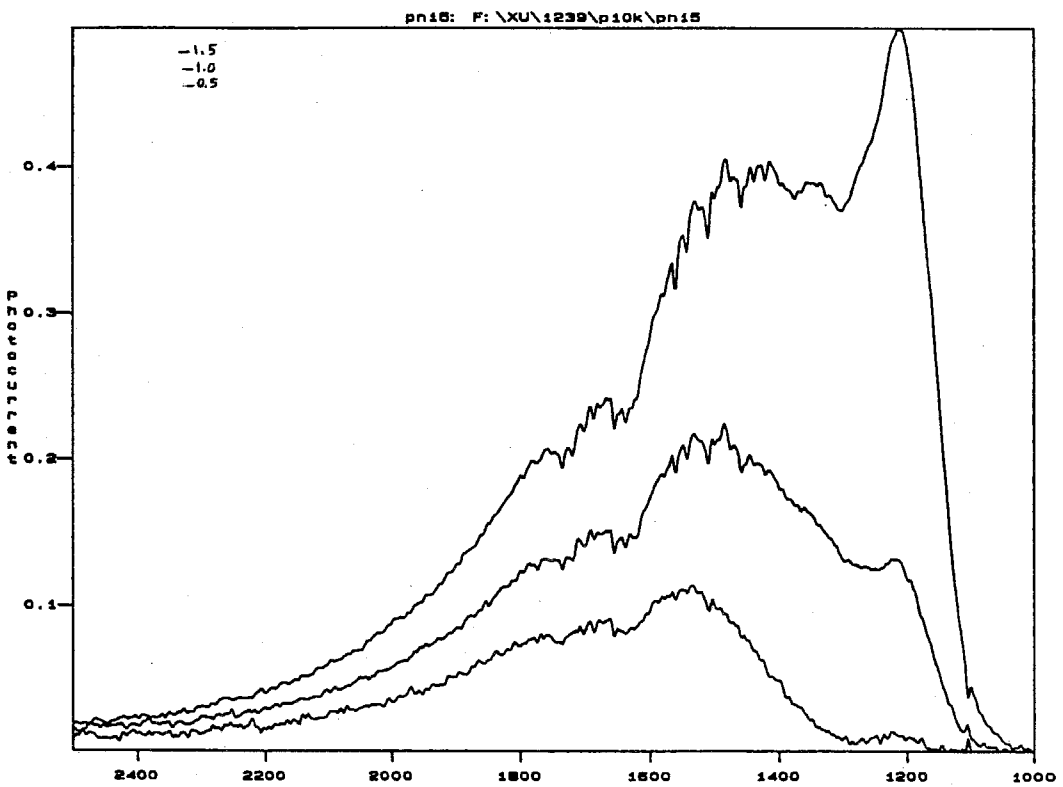

Figure 6-3: Photocurrent spectrum for smaller values of applied negative bias. Note the position of conduction band edge of $AlGaAs$ barrier, indicated on the figure.

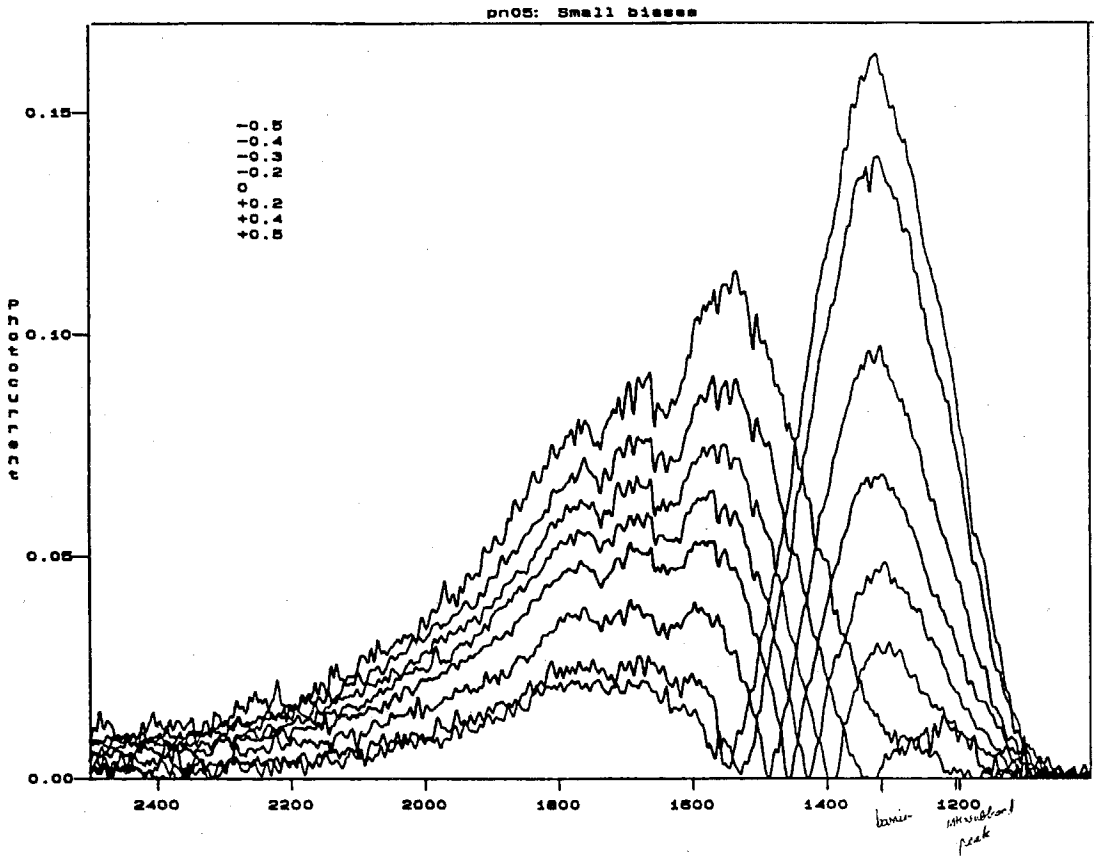

Figure 6-4: Photocurrent spectrum for very small values of applied bias, at a temperature of $10K$.

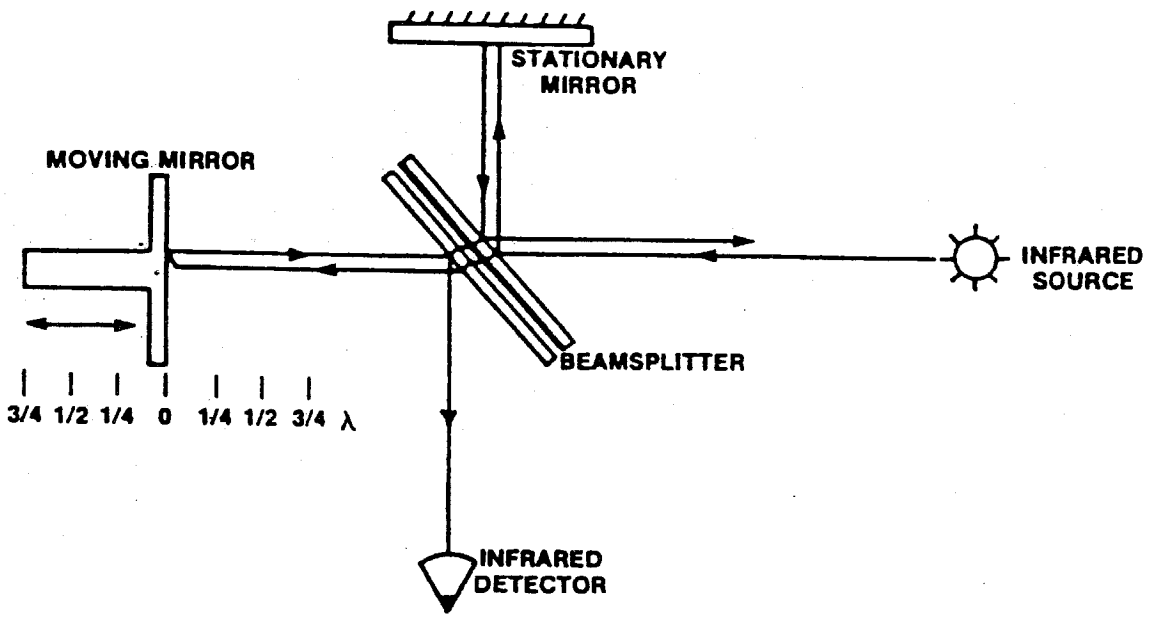

Figure 6-5: Michelson interferometer optical system

temperature of $10K$. Only for large biases can one see an appreciable photocurrent. This is because the photoexcited carriers in these bound-to-bound detectors need to tunnel out of the quantum wells to contribute to the photocurrent. Very thick barriers in this sample ($42.5nm$) require a large electric field to assist the electrons tunnelling out.

Figure 6-2 shows the photocurrent spectrum for several values of the applied negative bias (defined with respect to the bottom contact layer). As expected the spectrum has a narrow width ($\approx 15meV$), characteristic of bound-to-bound transitions. When the applied bias is smaller (see figure 6-3), the electron tunneling is greatly reduced, one can see more clearly the contribution of the states above the barrier (continuum states) to the photocurrent spectrum. The exact barrier height (conduction band edge of the AlGaAs layer), with respect to the quantum wells ground state energy, can be measured directly from this figure. One sees that the excited state in the well is $\approx 12meV$ below the conduction band in the barrier region.

At still lower biases (see figure 6-4) the photocurrent spectrum develops a strange

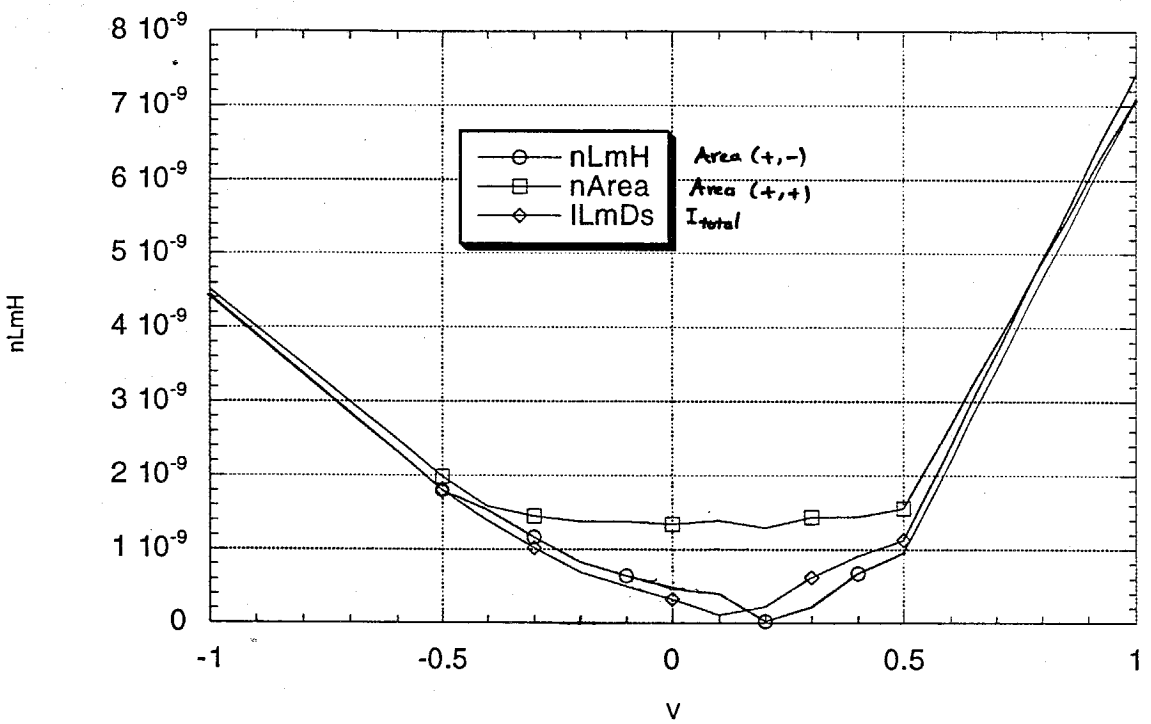

Figure 6-6: Comparison of the total photocurrent, integrated photocurrent, and the *sign adjusted* integrated photocurrent (i.e. The high energy photoexcited electrons moving in the opposite direction of the low energy ones).

(!) double peak. By changing the bias from $-0.5V$ to $+0.5V$, the high energy peak (at $\approx 1550 - 1700cm^{-1}$) is reduced while the low energy peak (at $\approx 1300cm^{-1}$) is increased.

The fact that in the energy range between these two peaks, the photocurrent spectrum goes to *zero*, was an indication that probably the sign of the photocurrent is not the same in the high and low energy part of the spectrum. In the following, we will look at the details of measuring the photocurrent spectrum with an FTIR spectrometer.

6.1.1 FTIR spectrometer

These photocurrent spectra were measured using the multiquantum well device as an external detector for a Fourier transform infrared (FTIR) spectrometer. FTIR is based on a Michelson interferometer in which one of the mirrors is moving (see figure 6-5). When the two light beams (one reflected from the stationary mirror and the other one reflected from the moving mirror) recombine at the beamsplitter, an interference pattern is generated. This pattern varies with the displacement of the moving mirrors and is detected by the infrared detector as variations in the IR energy level. In the case of monochromatic source light, as the the interferometer mirror scans back and forth, light and dark bands that correspond to constructive and destructive interference at the beam splitter, are observed by the detector (i.e. the detector response as a function of the mirror displacement, which is called the *interferogram*, will be a cosine function).

Infrared sources emit light over a broad range of frequencies, each frequency producing a unique cosine signal. The resulting interferogram represents the sum of the cosine waves. The frequency and intensity of each cosine wave in the interferogram is resolved by the Fourier transformation.

As we are using a black body source whose spectrum is almost constant in the frequency range of our analysis (1200 to $1800cm^{-1}$). The photocurrent spectrum

measured at the detector gives the frequency response of the detector itself. This detection scheme is not sensitive to the phase of the photocurrent generated (at least in its straightforward Fourier transformation). So this cannot produce the sign of the photocurrent, and what we see in the figure 6-4 is the absolute value of the photocurrent spectrum.

6.1.2 Integrated photocurrent

To check if there are both positive and negative components in the photocurrent spectra, we looked at the total photocurrent. This was directly measured by subtracting the detector currents in the presence of the IR source and without it. This total photocurrent was then compared with the integrated photocurrent, which was calculated from the measured spectra. The result is plotted in the figure 6-6. One can see that, as expected, for higher biases ($|V| > 0.5V$), the two curves of integrated and total photocurrent match very well over two orders of magnitude of current change. But in the voltage range $-0.5V$ to $0.5V$, the two curves differ by almost one order of magnitude.

If at small biases, the low energy photoexcited electrons move in the opposite direction to the ones having higher energies, their contribution should be subtracted to calculate the total photocurrent. In the figure 6-6, the integrated photocurrent, assuming different signs for the low and high energy peaks, more closely matches the measured total photocurrent. This indicates that effectively at small biases the photocurrent has two components one moving in the same direction as the applied bias and one moving in the *opposite* direction.

6.2 Explanation of the experimental results

The quantum well structure as designed, is symmetric with respect to the applied bias. But as it can be seen from figure 6-4, the negative bias photocurrent spectra

are different from the positive ones. This asymmetry is also seen in the current-voltage characteristics and has been reported by several other research groups [60,61,44,76] Intuitively, many factors may give rise to the asymmetry:

(a) An asymmetry in the height of the two barriers, from the unintentional asymmetries of the Al fraction during the growth.

(b) A difference in roughness of the two heterointerfaces confining a quantum well. It is commonly stated that the interface resulting from AlGaAs grown on GaAs (normal interface) is smoother than that of GaAs on AlGaAs (inverted interface)[54]. This is plausible due to the known lower atomic mobility of Al atoms versus Ga on the growing MBE surface.

(c) An asymmetry caused by impurity incorporation. The inverted interface incorporates more impurities (like oxygen), due to impurity surface segregation during AlGaAs growth followed by rapid incorporation in GaAs. This is plausible if we consider the competition for lattice sites between the impurities and the chemically very active Al.

(d) An asymmetry caused by segregation of the dopants during growth, which results in a spreading out of the dopants in the well regions and into the barriers[54]. The migration of dopant atoms in the direction of crystal growth is driven by a competition between Si and Ga (and Al in the case of the barrier), for the available Ga lattice sites.

Factor **(a)** is related to molecular beam flux transients commonly occurring on the opening of the cell shutters . The cell experiences a different environment when the shutter is closed than when it is open. This leads to a decrease in cell temperature, and therefore growth rate, with time. In our MBE system, the use of 1" spacers between the cells and growth chamber increases the distance between the shutter and the cell and has reduced the flux transients from 15% to 4%. For the growth of

the quantum wells the Aluminum shutter is only closed for about 15 seconds, so the expected flux transient is estimated to be less than 2%. This gives an asymmetry of the barriers of about $1meV$, which is negligible.

Factors **(b)** and **(c)** are difficult to model quantitatively. Moreover, it has been shown that Si segregation can explain 75 to 100% of the experimentally observed asymmetric I-V characteristics of the QWIPs. So focusing on factor **(d)**, we will see how the abnormal low bias behavior of the photocurrent spectrum could be explained.

6.2.1 Effect of Si-segregation on the quantum well band structure

Figure 6-7 shows the conduction band of the two periods of multiquantum well structure, which was calculated by self-consistently solving the Schrödinger and Poisson equations. The dopant segregation during the growth was taken into account by assuming an exponentially decreasing profile in one side of the barriers. The characteristic decay length of this exponential was taken to be $3nm$, consistent with values reported in the literature for Si-segregation during growth at a substrate temperature of $580°C$ [44,60].

Donor atoms in the barrier region are completely ionized and separated from their electrons which are trapped in the quantum wells. The separation between positive and negative charges produces internal electric fields which give an asymmetrical triangular shape to the barrier profile (see figure 6-7). It is the presence of these internal fields which make the photogenerated carriers go in a direction opposite to the applied bias. The reason the photogenerated carriers with different energies go in different directions can be explained as follows: The photogenerated carriers with energies below and close to the barrier height have wavefunctions mostly extended into the right-hand barrier. So that they will *feel* an average internal electric field pushing them toward the top of the sample. On the other hand, the high energy photoexcited carriers, having wavefunctions spreading over both right and left barriers, are swept

towards the substrate side of the sample (see figure 6-8).

This argument explains not only the behavior of photocurrent spectrum at small biases in our sample, but also the remarkable observation of the reference [59,60] having a device in which the photocurrent is actually opposite to the dark current. In their double barrier quantum well device (see figure 6-9), the presence of thin AlAs layers pushed the excited state of these detectors deep into the continuum. As the dark current is still dominated by the states near the AlGaAs barrier, because of Si-segregation, these two currents go in opposite directions.

6.3 Conclusion

It was seen that Si-segregation during the growth can explain the observed low bias spectrum of QWIPs. This spectrum was attributed to the fact that because of local electric fields, and different spatial extension of excited states, the photogenerated carriers with energies below and near the barrier edge are preferentially emitted towards the top side of the sample; while those excited with higher energies are transported towards the substrate side.

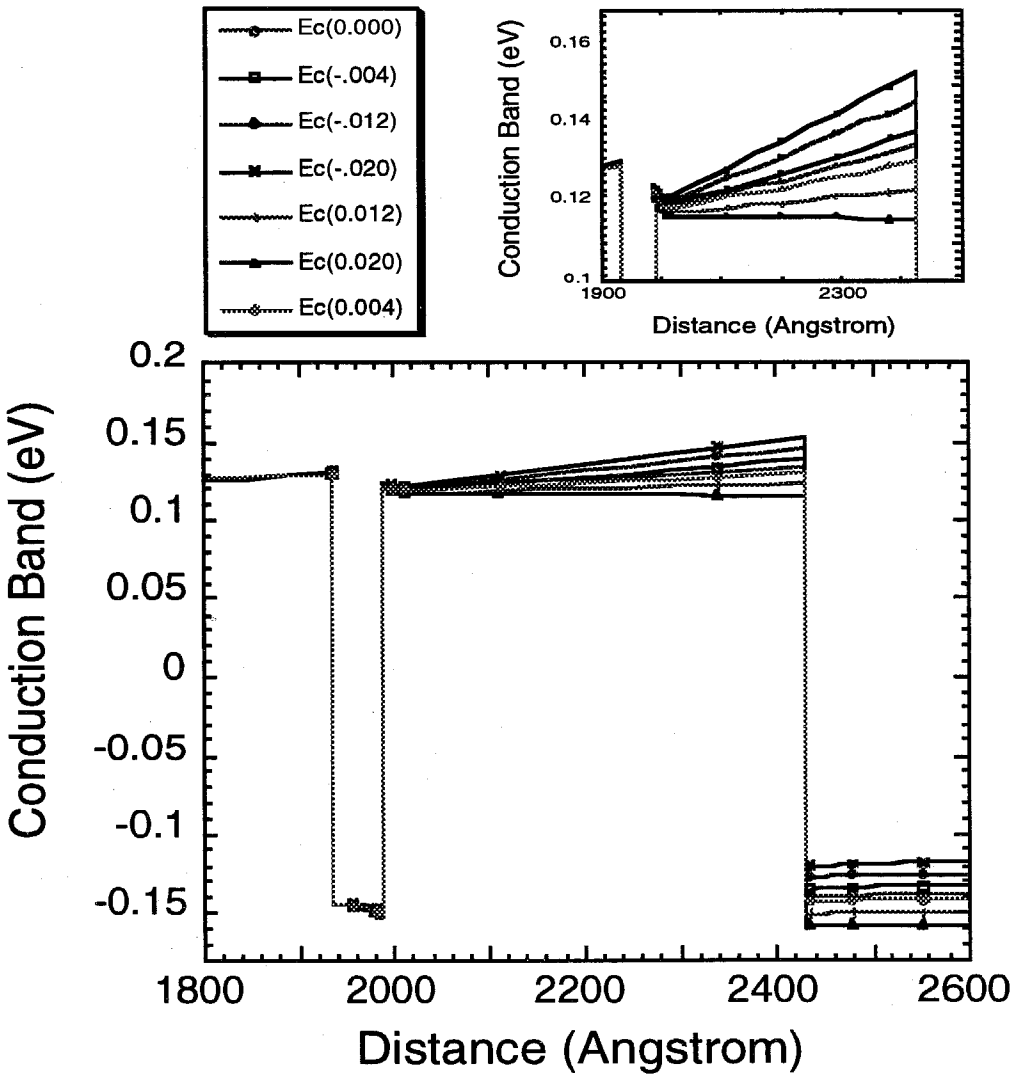

Figure 6-7: The calculated conduction band profile of two periods of the superlattice, assuming a Si-segregation of $3nm$ in the direction of growth (to the right).

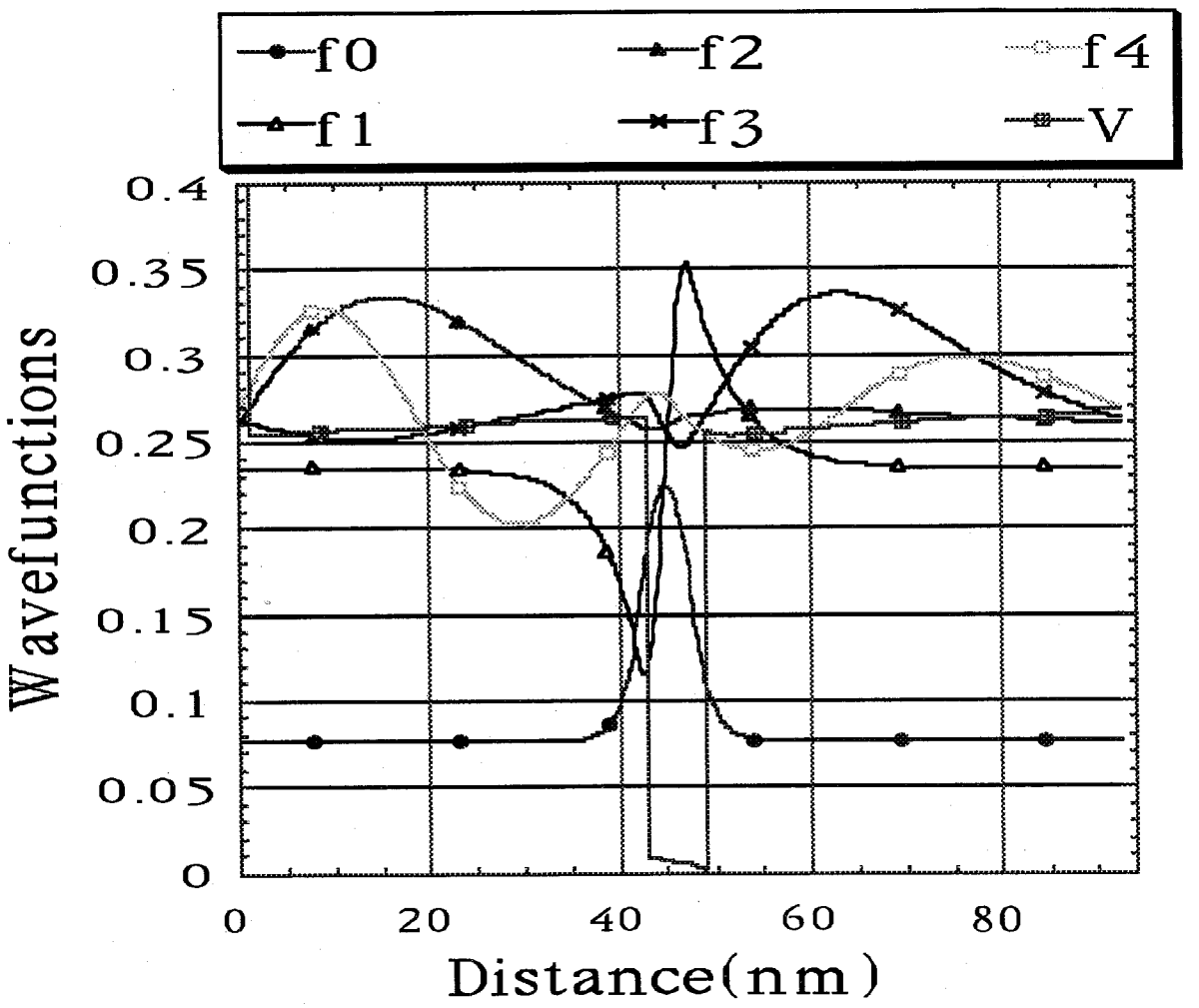

Figure 6-8: The calculated electronic envelope functions of the four lowest subbands for the potential profile of figure 6-7, at an applied bias of zero volts.

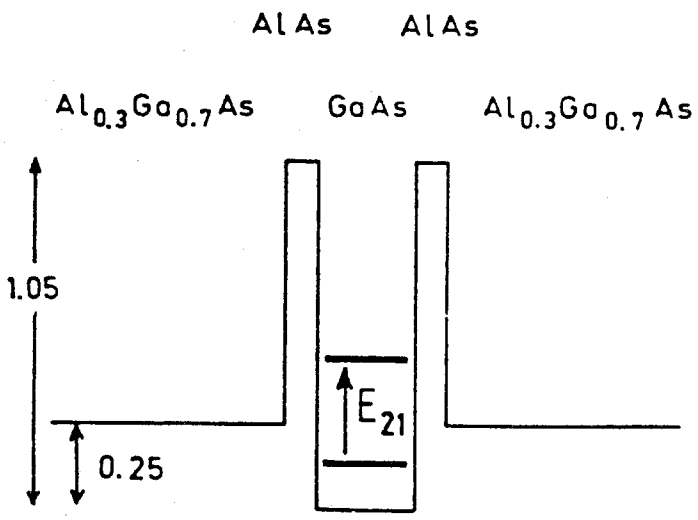

Figure 6-9: Conduction band profile and the position of energy levels in double barrier quantum well device of reference [58].

References

[1] M. Altarelli, 'Band structure, impurities and exciton in superlattices', in *Heterojunctions and semiconductor heterostructures*, edited by G. Allen, G. Bastard, N. Boccara, M. Lannoo, and M. Voos, 12 (Springer-Verlag, Berlin, 1986).

[2] G. Bastard, 'Wave mechanics applied to semiconductor heterostructures', *Les Editions de physique, France* (1988).

[3] M. Büttiker, and H. Thomas, 'Current instability and domain propagation due to Bragg scattering', *Phys. Rev. Lett.*, **38**,78 (1977)

[4] F. Capasso, K. Mohammad, and A.Y. Cho, 'Sequential resonant tunneling through a multiquantum well superlattice', *Appl. Phys. Lett.*, **48**, 478 (1986)

[5] F. Beltram, F. Capasso, D. Sivco, A.L. Hutchinson, S-N. G. Chu, and A. Cho, 'Scattering-controlled transmission resonances and negative differential conductance by field-induced localization in superlattices', *Phys. Rev. Lett.*, **64**, 3167 (1990)

[6] C. Sirtori, F. Capasso, J. Faist, and, S. Scandolo, 'Nonparabolicity and a sum rule associated with bound-to-bound and bound-to-continuum intersubband transitions in quantum wells', *Phys. Rev. B*, **50**, 8663 (1994)

[7] J. Faist, F. Capasso, A.L. Hutchinson, L. Pfeiffer, and K. West, 'Suppression of optical absorption by electric-field-induced quantum interference in coupled potential wells', *Phys. Rev. Lett.*, **71**, 3573 (1993)

[8] A. Cho, 'Molecular beam epitaxy',*American Institute of Physics* (1994).

[9] J.W. Choe, O. Byungsung, K.M.S.V. Bandara, and D.D. Coon, 'Exchange interaction effects in quantum well infrared detectors and absorbers', *Appl. Phys. Lett.*, **56**,1679 (1990).

[10] K.K. Choi, B.F. Levine, R.J. Malik, J. Walker and, C.G. Bethea, 'Periodic negative conductance by sequential resonent tunneling through an expanding high-field superlattice domain', *Phys. Rev. B* , **35**,4172 (1987)

[11] G. Dresselhaus, 'Spin-orbit coupling effects in Zinc blende structures', *Phys. Rev.*, **100**, 580-586 (1955).

[12] L. Esaki, and R. Tsu, 'Superlattice and negative differential conductivity in semiconductors', *IBM J. Res. Develop.*, **14**, 61 (1970).

[13] L. Esaki, and L.L. Chang, 'New transport phenomenon in a semiconductor superlattice', *Phys. Rev. Lett.*, **33**,495 (1974)

[14] D. Gershoni, J. Oknine-Schlesinger, E. Ehrenfreund, D. Ritter R.A. Hamm, M.B. Panish, 'Minibands in the continuum of multi-quantum-well superlattices', *Phys. Rev. Lett.* , **71**,2975 (1993)

[15] H.T. Grahn, H. Schneider and K. von Klitzing, 'Optical studies of electric field domains in GaAs/AlGaAs superlattices', *Phys. Rev. B*, **41**, 2890 (1990); H.T. Grahn, R.J. Haug, W. Muller, and K. Ploog, 'Electric field domains in semiconductor superlattices; a novel system for tunneling between 2D systems',*Phys. Rev. Lett.*, **67**, 1618 (1991)

[16] J.B. Gunn, 'Microwave oscillation of current in III-V semiconductors', *Solid. State. Commun.*, **1**,88,(1963); 'Instabilities of current in III-V semiconductors', *IBM J. Res. Dev.*,**8**, 141 (1964)

[17] A. Harwit, and J.S. Harris Jr., 'Observation of Stark shifts in quantum well intersubband transitions', *Appl. Phys. Lett.*, **50**,685 (1987).

[18] G.N. Henderson, L.C. West, T.K. Gaylord, C.W. Roberts, E.N. Glytsis, and, K. Ploog, 'Optical transitions to above-barrier quasibound states in asymmetric semiconductor heterostructures', *Appl. Phys. Lett.* , **62**,1432 (1993)

[19] M.A. Herman, and H. Sitter, 'Molecular beam epitaxy: fundamentals and current status',*Springer-Verlag* (1989).

[20] C. Hilsum, 'Transferred electron amplifiers and oscillators', *Proc. IRE*, **50**,185 (1962).

[21] H.J. Hutchinson, A.W. Higgs, D.C. Herbert, and G.W. Smith, 'Observation of miniband transport in $GaAs/Al_{0.33}Ga_{0.67}As$ superlattices', *J. Appl. Phys.*, **75**,320 (1994)

[22] A.A. Ignatov, K.F. Renk, and E.P. Dodin, 'Esaki-Tsu superlattice oscillator: Josephson-like dynamics of carriers', *Phys. Rev. Lett.*, **70**,1996 (1993)

[23] E.O. Kane, 'Band structure of Indium Antimonide', *J. Phys. Chem. Solids*, **1**, 249-261 (1957).

[24] E.O. Kane, *J. Phys. Chem. Solids*, **12**, 181 (1959).

[25] E.O. Kane, 'The **k.p** method', in *Semiconductors and semimetals, Vol. 1: Physics of III-V compounds*, eds. R.K. Willardson and A.C. Beer, 75 (1980).

[26] R.F. Kazarinov and, R.A. Suris, 'Electric and electromagnetic properties of semiconductors with a superlattice', *Sov. Phys. Semicond.*, **6**, 120 (1972);*ibid*, 'Possibility of the amplification of electromagnetic waves in a semiconductor with superlattice',*Sov. Phys. Semicond.*, **5**, 707 (1971)

[27] M.A. Kinch, and A. Yariv, 'Performance limitations of GaAs/AlGaAs infrared superlattices', *Appl. Phys. Lett.*, **55**,2093 (1989).

[28] J. Khurgin, 'Comparative analysis of the intersubband versus band-to-band transitions in qunatum wells', *Appl. Phys. Lett.*, **62**, 1390-1392 (1993).

[29] C. Waschke, H.G. Roskos, R. Schwedler, K. Leo, H. Kurz, K. Köhler, 'Coherent submillimeter-wave emission from Bloch oscillations in a semiconductor superlattice', *Phys. Rev. Lett.*, **70**, 3319 (1993)

[30] W. Kohn, J.M. Luttinger, 'Quantum theory of electrical transport phenomena', *Phys. Rev.*, **108**, 590 (1957).

[31] W. Kohn, 'Shallow impurity states in Silicon and Germanium', in *Solid state physics, Vol. 5*, eds. F. Seitz, and Turnbull, 257-320 (1957).

[32] H.J. Kreuzer, 'Theory of low temperature surface processes in epitaxy', in *Low temperature epitaxial growth of semiconductors*, Edited by T. Hariu, *World Scientific* , 1 (1991).

[33] L.B. Krieger, and G.J. Iafrate, 'Time evolution of Bloch electrons in a homogeneous electric field', *Phys. Rev. B* , **33**, 5494 (1986); G.J. Iafrate, in *Quantum transport in semiconductors*, Edited by D.K. Ferry, C. Jacoboni, *Plenum Press*, 53 (1992).

[34] H. Kroemer, 'Theory of Gunn effect', *Proc. IEEE*, **52**,1736 (1964).

[35] S.H. Kwok, R. Merlin, H.T. Grahn, and K. Ploog, 'Electric-field domains in semiconductor superlattices: Resonant and nonresonant tunneling', *Phys. Rev. B* , **50**,2007 (1994)

[36] B. Laikhtman and, D. Miller, 'Theory of current-voltage instabilities in superlattices', *Phys. Rev. B* , **48**,5395 (1993); B. Laikhtman, 'Current-voltage instabilities in superlattices', *Phys. Rev. B* , **44**,11260 (1991).

[37] D. Miller, B. Laikhtman, 'Theory of high-field-domain structures in superlattices', *Phys. Rev. B* , **50**,18426 (1994).

[38] B.F. Levine, R.J. Malik, J. Walker, K.K. Choi, C.G. Bethea, D.A. Kleinman, and J.M. Vandenberg, 'Strong 8.2 μm infrared intersubband absorption in doped GaAs/AlAs quantum well waveguides', *Appl. Phys. Lett.*, **50**,273,(1987).

[39] B.F. Levine, C.G. Bethea, K.K. Choi, J. Walker, and R.J. Malik, 'Bound-to-extended state absorption GaAs superlattice transport infrared detectors', *J. Appl. Phys.*, **64**,1591 (1988).

[40] B.F. Levine, G. Hasnain, C.G. Bethea and, N. Chand, *Appl. Phys. Lett.*, **54**,2704 (1989).

[41] B.F. Levine, C.G. Bethea, V.O. Shen, and R.J. Malik, 'Tunable long-wavelength detectors using graded barrier quantum wells grown by electron beam source molecular beam epitaxy', *Appl. Phys. Lett.*, **57**,383 (1990).

[42] G. Hasnain, B.F. Levine, C.G. Bethea, R.R. Abott, and S.J. Hsieh, 'Measurement of intersubband absorption in multiquantum well structures with monolithically integrated photodetectors', *J. Appl. Phys.*, **67**,4361 (1990).

[43] B.F. Levine, 'Quantum well infrared photodetectors', *J. Appl. Phys.*, **74**(8), R1 (1993).

[44] H.C. Liu, Z.R. Wasilewski, M. Buchanan, and H. Chu, 'Segregation of Si delta doping in GaAs-AlGaAs quantum wells and the cause of the asymmetry in the current-voltage characteristics of intersubband infrared detectors', *Appl. Phys. Lett.*, **63**,761 (1993).

[45] H.C. Liu, J. Li, Z.R. Wasilewski, M. Buchanan, P.H. Wilson, M. Lamm and J.G. Simmons, 'A three-color voltage tunable quantum well intersubband photode-

tector for long wavelength infrared', in *Quantum well intersubband transition physics and devices*, eds. H.C. Liu et al., 123 (1994).

[46] P. Löwdin, 'A note on the quantum-mechanical perturbation theory', *J. Chem. Phys.*, **19**, 1396-1401 (1951).

[47] J.M. Luttinger, and W. Kohn, 'Motion of electrons and holes in perturbed periodic fields', *Phys. Rev.*, **97**, 869-883 (1955).

[48] J.M. Luttinger, 'Quantum theory of cyclotron resonance in semiconductors: general theory', *Phys. Rev.*, **102**, 1030-1041 (1956).

[49] D. Calecki, J.F. Palmier, and A. Chomette, 'Hopping conduction in multiquantum well structures', *J. Phys. C*, **17**, 5017 (1984).

[50] J.F. Palmier, 'Miniband transport and resonant tunneling in superlattices', in *Resonant tunneling in semiconductors*, Edited by L.L. Chang, E.E. Mendez, C. Tejedor,*Plenum Publishing Corporation* ,361 (1990).

[51] A. Sibille, J.F. Palmier, H. Wang, and F. Mollot 'Observation of Esaki-Tsu negative differential velocity in GaAs/AlAs superlattices', *Phys. Rev. Lett.*, **64**,52 (1990); A. Sibille, J.F. Palmier,and F. Mollot,'Coexistance of Wannier-Stark localization and negative differential velocity in superlattices',*Appl. Phys. Lett.*,**60**,457 (1992).

[52] H. Le Person, C. Minot, L. Boni, J.F. Palmier, and F. Mollot, 'Gunn oscillations up to 20GHz optically induced in GaAs/AlAs superlattice', *Appl. Phys. Lett.*, **60**,2397 (1992).

[53] R.H. Parmenter, 'Symmetry properties of the energy bands of the Zinc blende structure', *Phys. Rev.*, **100**, 573-579 (1955).

[54] Loren Pfeiffer, E.F. Schubert, K.W. West, and C.W. Magee, 'Si dopant migration and the AlGaAs/GaAs inverted interface', *Appl. Phys. Lett.*, **58**,2258 (1991).

[55] B.K. Ridley, and T.B. Watkins, 'The possibility of negative resistance in solids', *Proc. Phys. Soc.*, **78**,293 (1961).

[56] E. Rosencher, E. Martinet, F. Luc, Ph. Bois, and E. Bockenhoff, 'Discrepancies between photocurrent and absorption spectroscopies in intersubband photoionization from GaAs/AlGaAs multiquantum wells', *Appl. Phys. Lett.*, **59**,3255 (1991).

[57] E. Martinet, F. Luc, E. Rosencher, Ph. Bois, and S. Delaitre, 'Electrical tunability of infrared detectors using compositionally asymmetric GaAs/AlGaAs multiquantum wells', *Appl. Phys. Lett.*, **60**,895 (1992).

[58] H. Schneider, F. Fuchs, B. Dischler, J.D. Ralston, and P. Koidl, 'Intersubband absorption and infrared photodetection at 3.5 and 4.2 μm in GaAs quantum wells', *Appl. Phys. Lett.*, **58**,2234 (1991).

[59] H. Schneider, K. Kheng, M. Ramsteiner, J.D. Ralston, F. Fuchs, and P. Koidl, 'Transport asymmetry and photovoltaic response in (AlGa)As/AlAs/ /GaAs/(AlGa)As single-barrier quantum-well infrared detectors', *Appl. Phys. Lett.*, **60**,1471 (1992).

[60] H. Schneider, E.C. Larkin, J.D. Ralston, K. Schwarz, F. Fuchs, and P. Koidl, 'Space charge effects in photovoltaic double barrier quantum well infrared detectors', *Appl. Phys. Lett.*, **63**,782 (1993).

[61] E.C. Larkin, H. Schneider, S. Ehret,J. Fleißner, B. Dischler, P. Koidl, and J.D. Ralston 'Influences of MBE growth processes on photovoltaic 3-5μm intersubband photodetectors', *IEEE Trans. Elec. Dev.*, **41**,511 (1994).

[62] F. Prengel, A. Wacker, and E. Schöll, 'Simple model for multistability and domain formation in semiconductor superlattices', *Phys. Rev. B* , **50**,1705 (1994); R.E. Kunz, and E. Schöll, 'Bistability and negative photoconductivity in optically induced real-space transfer', *Phys. Rev. B* , **47**,4337 (1993).

[63] I. Gravé, A. Shakouri, N. Kuze, and A. Yariv, 'Voltage-controlled tunable GaAs/AlGaAs multistack quantum well infrared detector', *Appl. Phys. Lett.*, **60**,2362 (1992).

[64] A. Shakouri, I. Gravé, Y. Xu, A. Ghaffari, and A. Yariv, 'Control of electric field domain formation in multiquantum well structures', *Appl. Phys. Lett.*, **63**,1101 (1993).

[65] G. Almogy, A. Shakouri, and A. Yariv, 'Observation of birefringence induced by intersubband transitions in quantum wells', *Appl. Phys. Lett.*, **63**,2720-2722 (1993).

[66] A. Shakouri,Y. Xu, I. Gravé, and A. Yariv, 'Electron transport, negative differential resistance and domain formation in very weakly coupled quantum wells', in *Quantum well intersubband transition physics and devices*, eds. H.C. Liu et al., 123 (1994).

[67] A. Shakouri,Y. Xu, I. Gravé, and A. Yariv, 'Electron transport, negative differential resistance and domain formation in very weakly coupled quantum wells', *Proceedings of the 21st International Conference on Compound Semiconductors* , (1994).

[68] Y. Xu, A. Shakouri, A. Yariv, A. Krabach, and T. Dejewski 'Direct measurement of doping density and barrier lowering effect with bias in quantum wells', *Elect. Lett.*, **31**, 320-321 (1995).

[69] Yuanjian Xu, Ali Shakouri, and Amnon Yariv, 'Quantum interference effects and electric field domain formation in quantum well infrared photodetectors', *Appl. Phys. Lett.*, **66**, 3307-3309 (1995).

[70] Ali Shakouri, Yuanjian Xu, and Amnon Yariv, 'Small bias behavior of quantum well infrared photodetectors', *In preparation.*

[71] A. Shik, 'Theory of optical intersubband transitions', in *Intersubband transitions in quantum wells*, eds. E. Rosencher, B.F. Levine, 319 (1992).

[72] M. Shur, 'GaAs devices and circuits', *Plenum Publishing Co.*, Ch.4 (1987).

[73] J. Singh, 'Physics of semiconductors and their heterostructures', *McGraw-Hill* (1993).

[74] J.S. Smith, L.C. Chiu, S. Margalit, A. Yariv, and, A.Y. Cho, 'A new infrared detector using electron emission from multiple quantum wells', *J. Vac. Sci. Technol. B*, **1**,376 (1983).

[75] S.M. Sze, 'Physics of semiconductor devices', 2nd edition, *Wiley & Sons publishers*, Ch.11 (1981).

[76] K.L. Tsai, C.P. Lee, K.H. Chang, D.C. Liu, H.R. Chen, and J.S. Tsang, 'Asymmetric dark current in quantum well infrared photodetectors', *Appl. Phys. Lett.*, **64**, 2436 (1994)

[77] R.Tsu, and G. Döhler, 'Hopping conduction in a superlattice', *Phys. Rev. B*, **12**, 680 (1975).

[78] G. Wannier, 'Wavefunctions and effective Hamiltonian for Bloch electrons in an electric field', *Phys. Rev.*, **117**,432 (1960).

[79] G.M. Williams, R.E. DeWames, C.W. Farley, and R.J. Anderson, 'Excess tunnel currents in AlGaAs/GaAs multiple quantum well infrared detectors', *Appl. Phys. Lett.*, **60**, 1324 (1992)

[80] Z.Y. Xu, V.G. Kreismanis, and C.L. Tang, 'Photoluminescence of GaAs-AlGaAs multiquantum well structures under high excitations', *Appl. Phys. Lett.*, **43**,415 (1983).